A spectroscopic analysis of Martian crater central peaks: Formation of the ancient crust

J. R. Skok,[1] J. F. Mustard,[1] L. L. Tornabene,[2] C. Pan,[3] D. Rogers,[3] and S. L. Murchie[4]

Received 31 May 2012; revised 17 August 2012; accepted 14 September 2012; published 7 November 2012.

[1] The earliest formed crust on a single plate planet such as Mars should be preserved, deeply buried under subsequent surface materials. Mars' extensive cratering history would have fractured and disrupted the upper layers of this ancient crust. Large impacts occurring late in Martian geologic history would have excavated and exposed this deeply buried material. We report the compositional analysis of unaltered mafic Martian crater central peaks with high-resolution spectral data that was used to characterize the presence, distribution and composition of mafic mineralogy. Reflectance spectra of mafic outcrops are modeled with the Modified Gaussian Model (MGM) to determine cation composition of olivine and pyroxene mineral deposits. Observations show that central peaks with unaltered mafic units are only observed in four general regions of Mars. Each mafic unit exhibits spectrally unmixed outcrops of olivine or pyroxene, indicating dunite and pyroxenite dominated compositions instead of basaltic composition common throughout much of the planet. Compositional analysis shows a wide range of olivine Fo# ranging from Fo_{60} to Fo_5. This variation is best explained by a high degree of fractionation in a slowly cooling, differentiating magma body. Pyroxene analysis shows that all the sites in the Southern Highlands are consistent with moderately Fe-rich, low-Ca pyroxene. Mineral segregation in the ancient crust could be caused by cumulate crystallization and settling in a large, potentially global, lava lake or near surface plutons driven by a hypothesized early Martian mantle overturn.

Citation: Skok, J. R., J. F. Mustard, L. L. Tornabene, C. Pan, D. Rogers, and S. L. Murchie (2012), A spectroscopic analysis of Martian crater central peaks: Formation of the ancient crust, *J. Geophys. Res.*, *117*, E00J18, doi:10.1029/2012JE004148.

1. Introduction

[2] The initial formation of a planetary crust is a critical stage in a planet's evolution. It can contain evidence of the last stages of planetary formation and gives a starting point for all subsequent crustal modification. The nature of this early crust is difficult to address on Earth as plate tectonics and other active geologic processes have destroyed, recycled or deeply buried and altered most of the ancient rocks. The lunar crust offers a well-studied primary crust [*Taylor*, 1992], thought to be formed by a plagioclase floatation process from a magma ocean [*Wood et al.*, 1970; *Warren*, 1990]. However, the small size and unique composition of the Moon makes it difficult to extrapolate this process to larger, wetter worlds. In this sense, Mars provides a valuable analog for the conditions of ancient terrestrial crusts with single-plate style of tectonics that would have preserved these crustal materials. Subsequently to ancient crust formation, Martian volcanism, alteration and impact cratering would obscure the ancient crust from surface observations. High-resolution observations from the Mars Reconnaissance Orbiter (MRO) can observe small, relatively compositionally pure outcrops of unaltered, igneous rocks that are exposed in crater central uplift structures as mega-block fragments, which may represent this ancient crust. This ancient crust of Mars is the key to understanding the formation and early evolution of the planet.

[3] The igneous composition of the current Martian surface has been studied by a number of investigations that use data from orbital, landed and laboratory instrumentation. With the possible exception of the Martian meteorite ALH84001 [e.g., *Mittlefehldt*, 1994; *Lapen et al.*, 2010] described below, all measurements of Martian lithologies are partially or entirely reprocessed after the planetary crustal formation. If the crustal blocks reported here are from this initial formational period, as we hypothesize, then we cannot directly compare them to previously reported results. However, the legacy of Martian igneous lithology observations detailed below illustrates the

[1]Department of Geological Sciences, Brown University, Providence, Rhode Island, USA.
[2]Department of Earth Sciences, University of Western Ontario, London, Ontario, Canada.
[3]Department of Geosciences, State University of New York at Stony Brook, Stony Brook, New York, USA.
[4]The Johns Hopkins University Applied Physics Laboratory, Laurel, Maryland, USA.

Corresponding author: J. R. Skok, Department of Geological Sciences, Brown University, 324 Brook St., Providence, RI 02912, USA. (john_skok@brown.edu)

0148-0227/12/2012JE004148

diversity of Martian volcanic processes and sets up the context for known Martian compositions.

[4] Global surface mineralogy was analyzed with the Thermal Emission Spectrometer (TES) [*Christensen et al.*, 1992] which mapped the presence and distribution of mafic minerals and igneous lithologies [e.g., *Bandfield et al.*, 2000; *Wyatt and McSween*, 2002; *Rogers and Christensen*, 2007; *Koeppen and Hamilton*, 2008]. Initial observations divided the primary crustal lithologies into a basaltic Surface Type 1 with 50% plagioclase feldspar, 25% clinopyroxene and 15% sheet silicates and an evolved Surface Type 2 with 35% plagioclase feldspar, 25% glass, 15% sheet silicates and 10% clinopyroxene with a hemispherical division between the types [*Bandfield et al.*, 2000]. Surface Type 2 has since been suggested that it is the result of an alteration process [*Wyatt and McSween*, 2002; *Ruff and Christensen*, 2007]. Surface Type 1 has been further refined to show specific compositions unique to individual volcanoes and regions [*Rogers and Christensen*, 2007]. Thermal analysis of olivine exposures show that the mineral makes up approximately 10–20% of the aggregate surface abundance [*Koeppen and Hamilton*, 2008]. Olivine detections have seen a range of compositions with a concentration at intermediate to forsteritic compositions (Fo_{68}-Fo_{53}) [*Koeppen and Hamilton*, 2008; *Hoefen et al.*, 2003] with some minor areas modeled with values as low as Fo_{39} and has high as Fo_{91} on a few basin rims. While TES provides the best available remote data set to determine global lithologies, the large, 3×6 km pixel resolution limits the ability to resolve crustal outcrops below the spatial resolution scale of this data set.

[5] Understanding of Martian surface mineralogy was further refined with visible and near infrared (VNIR) Observatoire pour l'Mineralogie, l'Eau, les Glaces, et l'Activite (OMEGA) observations (300 m to 5 km spatial resolution) mapping of iron-bearing igneous silicate mineralogy including high-calcium pyroxene (HCP), low-calcium pyroxene (LCP) and olivine [*Mustard et al.*, 2005; *Poulet et al.*, 2009]. The OMEGA observations confirmed and extended many of the TES results and greatly expand understanding of the aqueous alteration of the crust [*Bibring et al.*, 2006]. Additional studies have shown compositional trends with time as younger terrains having a relative enrichment in high-calcium pyroxene (HCP) [*Poulet et al.*, 2009; *Skok et al.*, 2010] and a depletion in SiO_2 [*Baratoux et al.*, 2011] hinting at the thermal evolution of the planet. However, the resolutions still result in large spatial averages of surface compositions.

[6] Small scale surface compositions have been determined in select locations by in situ analysis of Mars igneous samples with instrumentation on the Spirit Mars Exploration Rover [*Squyres et al.*, 2004]. An example is provided by the in situ analysis of Gusev basalts that have an estimated modal mineralogy of approximately 25% olivine, 30% pyroxene with the remaining as plagioclase and accessory minerals. In these basaltic rocks the olivine's cation composition was determined to be intermediate to mildly fayalitic ($Fo_{52–45}$) from the alpha particle x-ray spectrometer (APXS) measurements and $Fo_{60–35}$ based on MiniTES TIR observations [*McSween et al.*, 2006]. Additional exploration of the Columbia Hills, located near the center of Gusev Crater [*Squyres et al.*, 2006; *Arvidson et al.*, 2008] yielded deposits interpreted as pyroclastics [*Squyres et al.*, 2007] and materials consistent with an exposed hydrothermal system [*Squyres et al.*, 2008; *Ruff et al.*, 2011] suggesting a volcanic origin for the hills. An alternative explanation for the whole rock compositions is that they formed as a layered igneous intrusion with exposed harzburgite and olivine-norite and compositions ranging from $\sim Fo_{65}$-Fo_{45} [*Francis*, 2011].

[7] The most detailed analysis of Martian crustal composition is provided by the study of Martian Meteorites [e.g., *Mittlefehldt*, 1994; *Nyquist et al.*, 2001; *McSween*, 2002] These allow in-depth chemical analysis and a detailed petrographic history to be determined. Meteorite sampling has been skewed to only the most competent surface materials and therefore nearly all are relatively young, igneous rocks. The majority of the samples have been classified as basaltic Shergottites and have ages that range from 175 Ma to 475 Ma [*Nyquist et al.*, 2001, and references therein], indicating relatively recent Martian volcanic activity, though other analyze techniques suggest these samples could be as old as $\sim$4.0 Ga [*Bouvier et al.*, 2008]. However, the meteorites contain no contextual information, making it impossible to trace back the compositions to a particular region of Mars. Of particular interest is the meteorite, ALH84001, dated between 4.5 and 4.1 Gyr [*Mittlefehldt*, 1994; *Nyquist et al.*, 2001; *Lapen et al.*, 2010] depending on age determination method, it is the oldest sample of the Martian crust. The orthopyroxenite composition indicates the existence of early crustal processes capable of mineral segregation and may be a sample of a common early crustal component.

[8] Current understanding of the formation of Mars is determined from isotopic and petrologic observations from Martian meteorites [*Bertka and Fei*, 1997; *Debaille et al.*, 2007, and references within] and geophysical/geochemical modeling of planetary evolution [*Borg and Draper*, 2003; *Elkins-Tanton et al.*, 2005]. Isotopic studies show that the initial formation of Mars would progress rapidly with core formation having been largely completed 12.4 ± 4 Myr after solar system formation [*Debaille et al.*, 2007] while mantle evolution of source regions would be mostly completed within 100 Myr [*Debaille et al.*, 2007] (Figure 1). The details of this mantle evolution have been investigated with geophysical models. Magma ocean crystallization results have been predicted based a variety of magma ocean depths [*Borg and Draper*, 2003; *Elkins-Tanton et al.*, 2005]. Due to high energy release from early planetary formation processes we focus on the deep ocean process. *Elkins-Tanton et al.* [2005] describe the results from an early magma ocean that would crystalize olivine and pyroxene cumulates, beginning with Mg-rich minerals and progressing to Fe-rich as the melt cools. The resulting density inversion would be corrected with a planetary scale mantle overturn. The volcanic activity resulting for the overturn event would be responsible for the formation of the bulk of the earliest crust of Mars. This overturn model predicts a global crustal dichotomy where shallow cumulate melting would lead to voluminous magma, low-Al, and high Fo#, while deep melts would lead to less magma, higher-Al and $\sim Fo_{70}$ [*Elkins-Tanton et al.*, 2005]. These modeled predictions can now be tested with high-resolution spectroscopic images of the Martian surface.

[9] We focus this study on compositional determinations of 23 central peak exposures with unaltered, mafic spectroscopic signatures to investigate the nature of the buried, ancient Martian crust and compositional diversity across the planet (Figure 2 and Table 1). Note that we define "unaltered" as

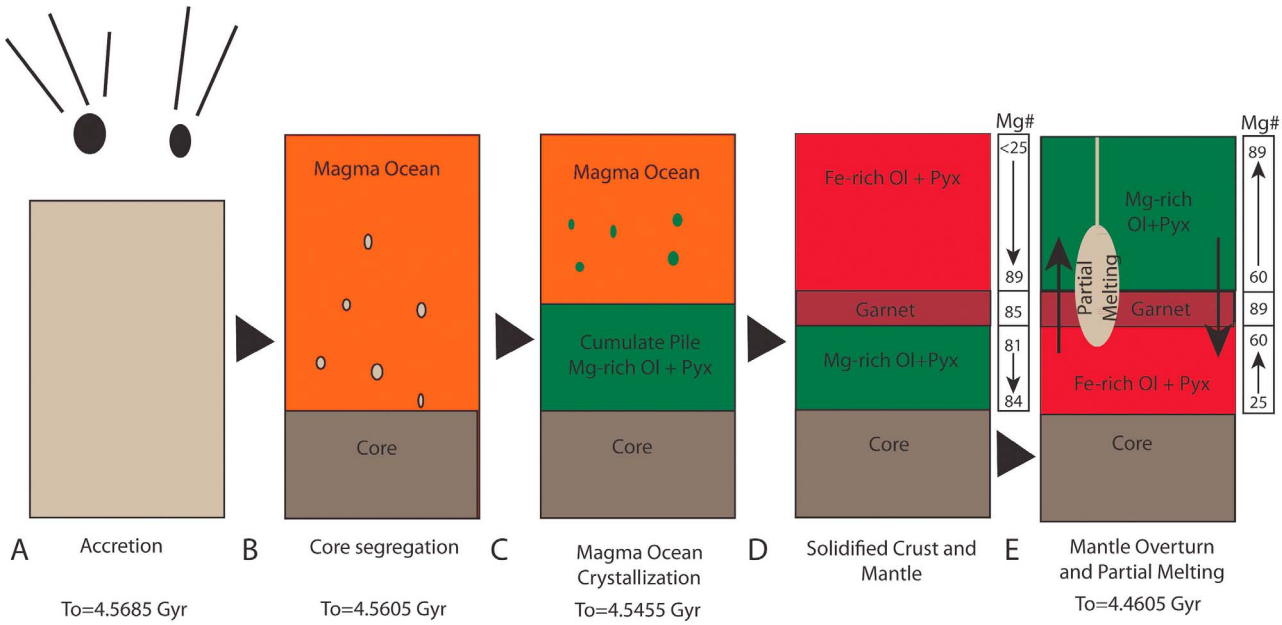

Figure 1. Planetary Formation Model. The best accepted model of Martian crustal formation combines our understanding of lunar formation, modeling of mineral crystallization and isotopic constraints from Martian meteorites. (a) Initial formation began with solar system condensation and accretion of meteoritic material. (b) Energy from impacts and differentiation would melt silicates forming a deep magma ocean and the segregation of metallic core. (c) Crystallization of the magma ocean would begin with Mg-enriched olivine and later pyroxenes that would be denser than the melt and forming a cumulate pile at the bottom of the magma ocean and result in an increasingly Fe-rich magma. (d) Crystallization would end with Fe-rich olivine and pyroxenes above a garnet layer stable at depths of 1050 km. The water content of the magma would suppress plagioclase formation. (e) The mineral crystallization sequence would create a density inversion that would be corrected with an overturn that is likely to be continuous with the crystallization of the Fe-enriched minerals. The displacement of the Mg-rich minerals toward spatially higher and lower pressure regions would result in decompression partial melting. The final stages of this process, occurring after the majority of the magma ocean has crystallized, would extrude on the ancient Martian surface and form the bulk of the Martian Crust. (Based on *Debaille et al.* [2009] and *Elkins-Tanton et al.* [2005]).

spectral units that do not exhibit significant hydrous or hydroxylated phases at the spatial scale of the CRISM data. These observations are then integrated into a model for the formation of the ancient crust that can be used to refine and test future planetary formation models.

2. Analysis Techniques

[10] To develop the database of exposed, unaltered crust on Mars for analysis, we considered all potential central peak exposure observations. The survey initially considered ~150 sites included in the Crater Exposed Database compiled by *Tornabene et al.* [2010], which characterized central features in craters on the basis of High Resolution Imaging Science Experiment (HiRISE) [*McEwen et al.*, 2007] and Context Imager (CTX) [*Malin et al.*, 2007] morphological data. Of these 105 had full resolution targeted (FRT) observations from the Compact Reconnaissance Imaging Spectrometer for Mars (CRISM) instrument [*Murchie et al.*, 2007]. FRTs of central peaks were first examined with spectral summary parameter maps [*Pelkey et al.*, 2007] that quickly summarize where likely exposures of unaltered crust exist. To confirm that in fact alteration minerals (identified on the basis of 1.9 μm H_2O combination tone) are absent and that crystalline igneous mafic minerals, olivine and/or pyroxene are present in bedrock exposures the areas highlighted in spectral summary parameters were examined in detail with the full resolution spatial and spectral CRISM data. Observations with strong spectral signatures were then used to guide the selection of multipixel regions of interest (ROI). ROIs are selected based on regions highlighted in the mafic summary spectral parameters with associated ratio denominators selected in the same columns in a region of bland mafic parameters, typically in the crater floor. The result was the 23 crater central peaks have CRISM observation, mafic spectral signatures and negligible alteration.

[11] On Mars, crustal exposures occur in three major types of environments; outflow channels [*Rogers et al.*, 2005; *Loizeau et al.*, 2010], tectonic rifting such as in Valles Marineris [*Flahaut et al.*, 2011], and impact craters [*Melosh*, 1989; *Baratoux et al.*, 2007; *Cahill et al.*, 2009; *Tornabene et al.*, 2010]. Of these, impact craters are the most globally pervasive with the deepest excavated materials typically exposed in the central peak structures [*Melosh*, 1989]. The vertical relief of central peaks is the key to preserving the strong spectral signatures by allowing surface refreshing and preventing crater fill from obscuring the observations. Since we require compositional analysis capable of distinguishing multiple

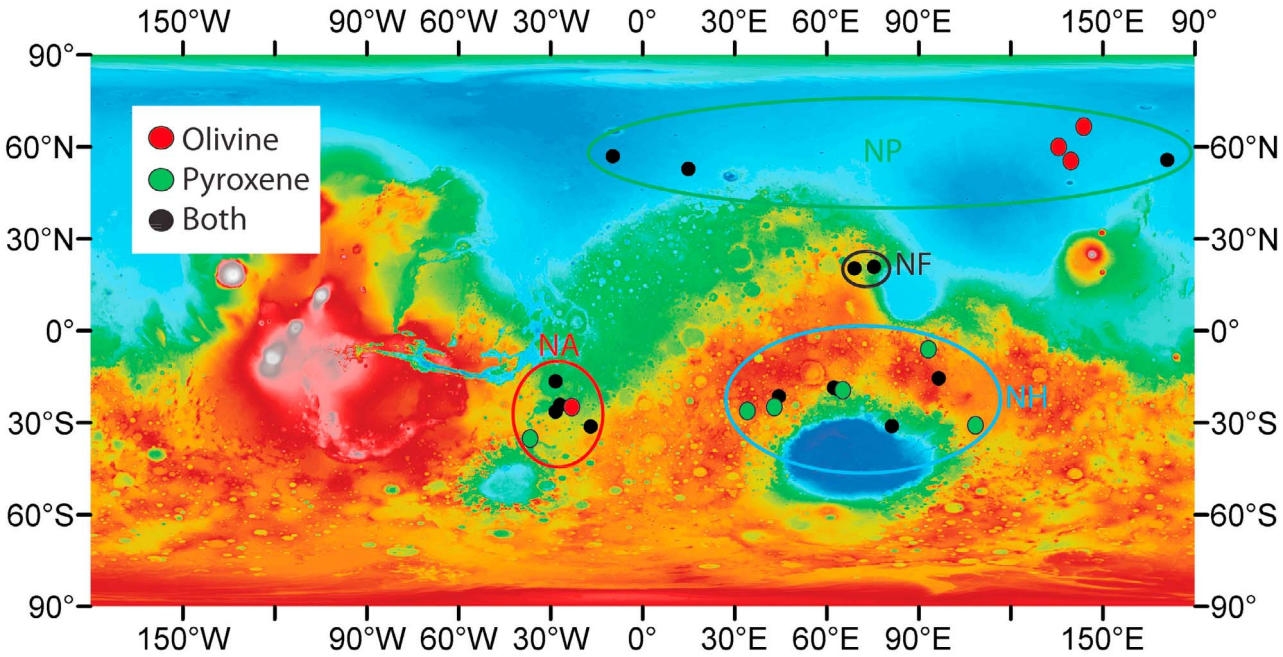

Figure 2. Map of Analyzed Sites. Twenty-three sites have unaltered mafic spectra that can be modeled with the MGM. The result of this selection process is a natural grouping in four general regions, North Argyre (NA), North Hellas (NH) Nili Fossae (NF) and Northern Plains (NP). Red marks have only olivine outcrops, Green marks have only pyroxene outcrops, Black marks have both olivine and pyroxene outcrops. (MOLA color DEM background).

lithologies within these peaks, we will use spectral data from the CRISM instrument to identify, map and analyze the central peak units. Multispectral, 100 m/pixel resolution data from the Thermal Emission Imaging System (THEMIS) instrument [*Christensen et al.*, 2004] are also used to compliment and interpret the CRISM-based spectral mapping of craters peaks in Alga and Ostrov Crater. Morphology of both central peaks was analyzed with HiRISE 25 cm/pixel imagery. Stereo

Table 1. Details From Each of the Central Peak Structures Reported in This Study[a]

Code	Name	CRISM ID	Latitude	Longitude	Diameter	Olivine	Pyroxene
NA1	Alga Crater	2007_167_6415	−24.34	−26.65	18	O	P
NA2	Ostrov Crater	2010_099_17D02	−26.51	−28.09	70	O	P
NA3	Hale Crater	2009_066_117BC	−35.58	−36.43	130	O	P
NA4	**Ladon Basin**	2008_018_97FF	−16.71	−28.14	22	O	P
NA5	**Kasimov Crater**	2008_186_B5BE	−24.93	−22.78	7	O	-
NA6		2009_042_10FE8	−31.41	−16.66	37	-	P
NH1		2009_042_C2A5	−25.78	34.42	39	-	P
NH2		2008_032_9BCF	−24.26	43.47	22	-	P
NH3		2008_248_C554	−18.74	62.63	50	O	P
NH4		2009_231_147FB	−21.53	44.75	42	O	P
NH5		2011_173_1EB32	−19.32	64.03	31	-	P
NH6		2011_176_1EBA0	−31.43	81.63	20	O	P
NH7		2010_086_177F9	−6.23	93.63	26	-	P
NH8		2007_286_82E8	−15.75	96.87	35	O	P
NH9		2008_245_C4D0	−31.29	108.67	73	-	P
NF1	Hargraves Crater	2008_185_B573	20.76	75.81	62	O	P
NF2		2009_044_110B7	20.22	69.42	50	O	P
NP1	Kunowsky Crater	2008_013_9610	56.86	−9.23	62	O	P
NP2		2010_127_18A06	52.64	15.24	25	O	P
NP3		2008_242_C417	59.84	135.80	30	O	-
NP4		2008_232_C16F	55.58	139.65	26	O	-
NP5	Stokes Crater	2008_155_ADA4	55.65	171.35	63	O	P
NP6		2010_093_17AA1	66.42	144.06	29	O	-

[a]Column Key: Code: Central peak designation for this project. Letters refer to region, NA: North Argyre, NH: North Hellas, NF: Nili Fossae, NP: Northern Plains. Number is based on analysis order. Name: Name of crater where available, bold name indicates that the examined cater is an unnamed crater within the larger named crater in bold. CRISM_ID: Is a concatenation of CRISM FRT information as: Obs Year_Obs Day_Obs Hexidecimal ID. Longitude has positive values going east. Diameter is the average diameter of the observed crater. Olivine and Pyroxene are marked if that mineral has been modeled at that site.

HiRISE [*McEwen et al.*, 2007] observations of the Alga central peak were processed into a digital elevation model [*Kirk et al.*, 2008] that allowed determination of precise 3D perspectives.

[12] *CRISM*. The primary data set used in this study was observations from the CRISM VNIR hyperspectral imaging instrument [*Murchie et al.*, 2007]. CRISM acquires full resolution targeted (FRT) images at 18 m per pixel spatial resolution and 544 spectral bands ranging from 0.32 – 4.0 μm. CRISM observations were corrected for instrumental artifacts and were converted into I/F [*Murchie et al.*, 2007]. To use the observations on surface mineral measurements, a simple multiplicative correction was used to remove the atmospheric contribution to the spectra. This was determined using a volcano scan method developed and tested on ISM [*Bibring et al.*, 1989] and OMEGA [*Mustard et al.*, 2005]. A detailed description of the volcano scan method is in *McGuire et al.* [2009]. The CRISM data are collected on a short wavelength S-detector (VNIR: 362–1053 nm) and a long wavelength L-detector (IR: 1002–3920 nm). Full wavelength modeling requires detector coordination. Ratioed spectra were calculated for each detector independently, then joined by removing the overlapping spectral data (1000 nm – 1053 nm) from the S-detector data and including an additive scaling factor on the S-detector data to match the value of the minimum wavelength of the L-detector [*Murchie et al.*, 2007]. The absolute value of the ratioed value is dependent on the relative albedo of the region of interest and denominator area and does not affect modeling as long as the values are consistent between detectors. Mafic mineral deposits are identified with mafic parameter maps that highlight spatial regions with characteristic spectral absorptions [*Pelkey et al.*, 2007; *Salvatore et al.* 2010]. The parameter equations used to identify olivine, low-Calcium pyroxene (LCP) and high-Calcium pyroxene (HCP), respectively, are given below:

OLINDEX2:

$$\left(\left(\frac{RC1054 - R1054}{RC1054}\right) * 0.1\right) + \left(\left(\frac{RC1211 - R1211}{RC1211} * 0.1\right) + \left(\left(\frac{RC1329 - R1329}{RC1329}\right) * 0.4\right) + \left(\left(\frac{RC1474 - R1474}{RC1474} * 0.4\right)\right)\right) \quad (1)$$

LCPINDEX:

$$\left(\frac{R1330 - R1050}{R1330 + R1050}\right) * \left(\frac{R1330 - R1815}{R1330 + R1815}\right) \quad (2)$$

HCPINDEX:

$$\left(\frac{\mathrm{R1470} - \mathrm{R1050}}{\mathrm{R1470} + \mathrm{R1050}}\right) * \left(\frac{\mathrm{R1470} - \mathrm{R2067}}{\mathrm{R1470} + \mathrm{R2067}}\right) \quad (3)$$

Where R#### is the reflectance value at #### nm and RC#### denotes the value of a point at a wavelength of #### nm along a modeled line that follows the average slope of the spectrum. Average spectra were collected from regions of interest in the mineral deposits and were ratioed to a spectrally bland region in the same column of pixels, typically in the crater floor fill.

[13] *MGM Method*. The modified Gaussian method (MGM) [*Sunshine et al.*, 1990] was used to estimate the cation compositions of the minerals olivine and pyroxene (Figure 3). The MGM deconvolves overlapping absorptions of mafic mineral spectra into their fundamental absorption components. Individual absorption components are modeled as modified Gaussian distributions that mathematically describe the specific shape of electronic transition absorptions and are parameterized by a band center, band width, and band strength. The MGM models a spectrum's absorption features with Gaussian distributions and relates them to known absorption features. Gaussians are defined as:

$$g(x) = s * \exp\left(-\frac{(x-\mu)^2}{2\sigma}\right) \quad (4)$$

where s is band strength, σ is the band width, and μ is the band center. The MGM superimposes several Gaussians onto a continuum to model the spectrum with known absorption features at fixed wavelengths due to specific electronics transitions, discussed further below. MGM computations are carried out in energy and natural log reflectance space and thus overlapping absorptions are additive and can be modeled using linear inverse theory [*Sunshine et al.*, 1990]. The inversion method applied in *Sunshine et al.* [1990] is the stochastic inversion of *Tarantola and Valette* [1982] that allows for the inclusion of a priori information as constraints on the solutions. *Sunshine and Pieters* [1993] showed that the constraints helped to stabilize the inversion process and prevent physically unrealistic solutions. The inversion is an iterative process and all absorption band parameters and the continuum are free to move until the residual errors between the log of the actual spectrum and the log of the modeled spectrum are less that 10^{-5} between consecutive model runs [*Sunshine et al.*, 1990].

[14] Initial MGM development was performed on laboratory measurements of pyroxenes [*Sunshine et al.*, 1990; *Sunshine and Pieters*, 1993] with later development using laboratory measurements with a range of olivine compositions [*Sunshine and Pieters*, 1998]. MGM has since been used on laboratory measurements of lunar olivine [*Isaacson and Pieters*, 2010], remotely sensed lunar olivine from the M^3 instrument [*Isaacson et al.*, 2011], laboratory and remotely Martian pyroxenes [*Kanner et al.*, 2007; *Skok et al.*, 2010], remote terrestrial observations [*Combe et al.*, 2006] and Martian mafic mixtures from OMEGA observations [*Clénet*, 2011]. This investigation is the first full treatment of CRISM data using the MGM for compositional determination. Initial selection of Gaussian absorption properties (band center, band width, and band strength) was determined based on knowledge of the spectral properties of mafic minerals (Table 2) [*Burns*, 1993; *Sunshine and Pieters*, 1993, 1998], and the model was then allowed to automatically modify these values to produce the best fit to the observed spectrum. In cases where the automatic fitting routine failed to provide a satisfactory fit, attempts were made to refine the fit by first fitting a continuum curved in energy space [*Hiroi and Sasaki*, 2001] before allowing freedom of the individual band absorptions.

[15] *Olivine Analysis*. Olivine ($(Mg, Fe)_2SiO_4$) is a magnesium-iron silicate with a nesosilicate structure. It is spectrally identified in the near-infrared by a broad absorption centered near 1 μm that is the superposition of three

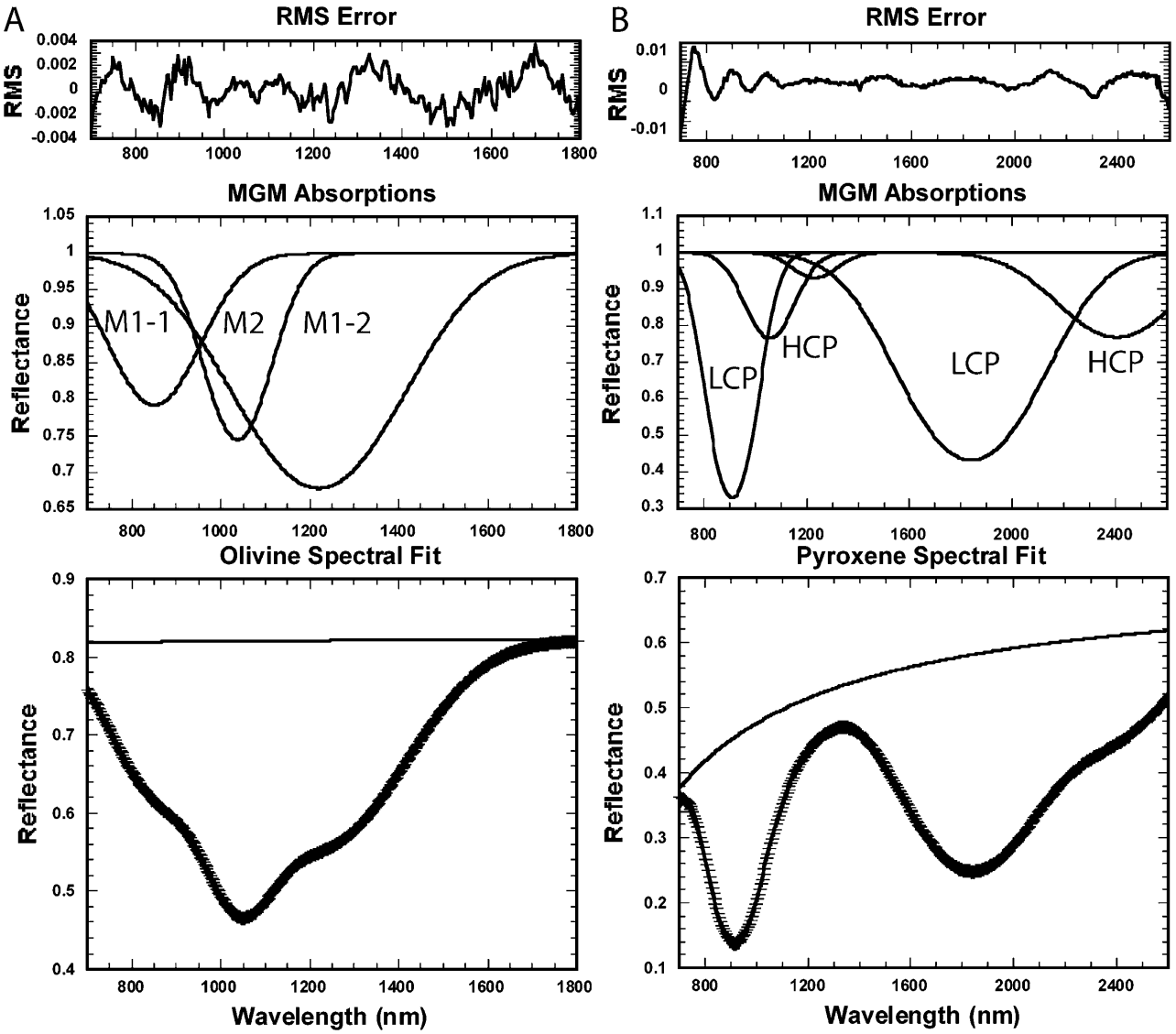

Figure 3. MGM Example. (a) MGM run on laboratory Olivine with Fo # 96 (Relab sample: c3po53). (top left) RMS error between the observed spectra and modeled fit. (middle left) Three olivine absorptions with fitted positions, widths, and strengths. Initial positions, depths and widths are listed in Table 1. (bottom left) Olivine spectra (cross hatched points) with fit (black line) and curved continuum (thin black line). (b) MGM run on laboratory Pyroxene (Relab Sample: c1xp23). (top right) RMS error between the observed spectra and modeled fit. (middle right) Five absorptions with fitted positions, widths, and strengths. (bottom right) Pyroxene spectra (cross hatched points) with fit (black line) and curved continuum (thin black line).

overlapping absorptions caused by electronic transitions in Fe^{2+} ions located in distorted octahedral crystal lattice sites [*Burns*, 1970, 1974, 1993]. The exact band center of each of these absorptions is related to the relative proportion of Fe and Mg in the M1 and M2 sites with increasing Mg causing shorter wavelength absorptions and increasing Fe causing longer wavelength absorptions [*Burns*, 1970; *King and Ridley*, 1987; *Sunshine and Pieters*, 1998]. To avoid spectral effects outside the diagnostic 1 μm band, we only model from 0.8 μm to 1.8 μm but visually check that there are no 2 μm spectral features related to pyroxene. Three bands are used to model this absorption (Table 2) with the resulting fitted band centers determining the composition [*Sunshine*

Table 2. List of Initial MGM Modeled Absorption Properties[a]

Absorption Feature	Band Center (μm)	Band Width (μm)	Band Depth
Olivine M1–1	0.9	0.228	−0.08
Olivine M2	1.08	0.176	−0.08
Olivine M1–2	1.28	0.424	−0.08
Pyroxene 1 μm	1.0	0.288	−0.08
Pyroxene 2 μm	2.0	0.424	−0.08
Pyroxene 1 μm LCP	0.9	0.228	−0.08
Pyroxene 1 μm HCP	1.08	0.228	−0.08
Pyroxene 1.2 μm	1.28	0.176	−0.08
Pyroxene 2 μm LCP	1.9	0.424	−0.08
Pyroxene 2 μm HCP	2.3	0.424	−0.08

[a]Band strength in natural log reflectance.

and Pieters, 1998; *Isaacson and Pieters*, 2010]. To determine the composition of a given spectrum, the three band centers are fit to a laboratory derived compositional trend line to fit for least error using the following relationship [*Isaacson and Pieters*, 2010].

$$A = \left[\frac{1112.3}{1.2179^2} + \frac{2373}{2.2^2} + \frac{1335.9}{1.0309^2}\right] \quad (5)$$

$$B = \left(\frac{1}{1.2179^2} + \frac{1}{2.2^2} + \frac{1}{1.0309^2}\right) \quad (6)$$

$$Fo = B^{-1} * \left[A - \left(\frac{M1-1}{1.2179^2} + \frac{M2}{2.2} + \frac{M1-2}{1.0309}\right)\right] \quad (7)$$

where A and B are constants that constrain the slope of the experimentally determined compositional relationship that relates the composition of the olivine to the band center for each of the three olivine absorptions. M1–1, M2, and M1–2 represent the band centers (in nm) for the three olivine absorptions. Fo is the cation composition ratio of Mg wt.% / (Mg wt.% + Fe wt.%) ranging from 0 (100% Fe) to 100 (100% Mg).

[16] The formula can be modified to be fit to any two band inputs if needed. When modeling CRISM data we found that limiting analysis to the L detector data produces most reliable results because of the L + S detector alignment. The natural properties of the long wavelength M1–2 feature gives it the most wavelength variability per change in composition, meaning that small changes in bandcenters will have the least effect on the modeled composition making it the most stable feature band to fit. For these reasons, we include the modeled fits both using all three olivine bands and alternatively only using the M2 and M1–2 bands.

[17] The MGM analysis of olivine was initially shown to be independent of grain size [*Sunshine and Pieters*, 1998], but subsequent work has detected a dependence in laboratory spectra of particulates [*Clénet et al.*, 2011]. The precise nature of this dependence is still an active source of research and of questionable applicability for spectra measurements of crystalline material with interlocking crystals with no space between crystal faces, creating a much different reflection path than in particulate material.

[18] *Pyroxene Analysis*. Pyroxene ((Ca, Mg, Fe)Si_2O_6) is spectrally identified by absorptions at 1 and 2 μm with the band center slightly dependent on the Mg-Fe cation content and strongly dependent on the Ca content [*Adams*, 1974; *Cloutis et al.*, 1986; *Cloutis and Gaffey*, 1991; *Klima et al.*, 2007] and a weak 1.2 μm absorption. The pyroxene absorptions are caused by crystal field transitions of iron in octahedral coordination with the 1- and 2-μm absorptions due to the composition of the M2 crystallographic site. This causes distortion in the crystal structure based on the size of the cation. The 1.2 μm absorption is due to molecular distortion in the M1 crystallographic site [*Burns*, 1993]. Pyroxene Ca content can be determined by modeling each absorption as a combination of end-member low-calcium and high-calcium pyroxenes. *Kanner et al.* [2007] has shown that the ratio of modeled end-member absorption strengths is proportional to the relative composition of each end-member. Since pyroxene composition is spectrally distinguished by the Ca content, we refer to high-Ca (HCP) and low-Ca (LCP) compositions. This spectral determination does not directly distinguish structural variants of orthropyroxene (OPX) and clinopyroxene (CPX). However, in practice LCP strongly coincides with OPX and may indicate enstatite or pigeonite while HCP coincides with CPX, typically augite or diopside. Pyroxene is modeled in two ways. The first is with 5 absorptions (Table 2); the LCP and HCP end-members of both the 1 and 2 μm absorptions and an absorption at 1.2 μm are used to provide a reliable fit but not used to determine composition. Relative Ca content is determined by ratioing the modeled LCP end-member band strength by the combination of the LCP and HCP strength, LCP/(LCP + HCP) determining the normalized band strength ratio (NBSR) [*Kanner et al.*, 2007]. This is done for both the 1 and 2 μm absorptions. A value of 1.0 indicates there is only LCP while a value of 0.0 indicates only HCP, with intermediate values proportional to the relative Ca content. The second way pyroxene is modeled is with a single 1 and 2 μm absorption to calculate the overall band centers for classification against terrestrial pyroxenes.

[19] *MGM Error Consideration*. MGM was developed and tested by analyzing laboratory spectral measurements of well-characterized samples. Olivine compositional error occurs at two separate steps. The first is during the MGM spectral fitting process that models the CRISM spectra with the Gaussian absorptions. The model is running until the RMS increases less than 10^{-5} with a successive iteration and is always lower than 10^{-2}. However, errors from slight variations in initial spectral parameters lead to an error of $\sim\pm5$ Fo# for olivine [*Isaacson and Pieters*, 2010]. Additional errors are expected when applying the MGM to remote sensing data with lower signal-to-noise and additional spectral components. The second step is the calculation of Fo# from the modeled band-centers. *Isaacson and Pieters* [2010] determined a composite error for the MGM of olivine with the M3 data set to be $\sim\pm20$ relative Fo# units. The composition is calculated as a least squares fitting to either 3 or 2 slopes. The greater the difference between the laboratory determined slopes and actual data the larger the error in the compositional determination. This error in the determination of the precise composition of a single unit spectral average encourages the use of the modeled results to determine general ranges and regional trends instead of the exact composition of a single exposure. A separate study applying the MGM to pyroxenes with laboratory and OMEGA data determined that the calcium content can be constrained to $\pm10\%$ [*Kanner et al.*, 2007].

[20] *Thermal Infrared*. We use the multispectral thermal infrared observations from the Thermal Emission Imaging System (THEMIS) instrument [*Christensen et al.*, 2004] to provide an independent check on the composition. THEMIS operates both a TIR multispectral mode with nine bands between from 6.8 to 14.9 μm with 100-m per pixel resolution and a visible mode with five bands and 18-m per pixel resolution. Hyperspectral observations from the TES instrument were examined for both the Alga and Ostrov central peaks. Alga's central peak did not have high quality data coverage. A few TES spectra were available for Ostrov's central peak; however these were determined to have artifacts invalidating mineral determinations.

[21] THEMIS daytime multispectral images with warm (>265 K) surface temperatures were selected for detailed

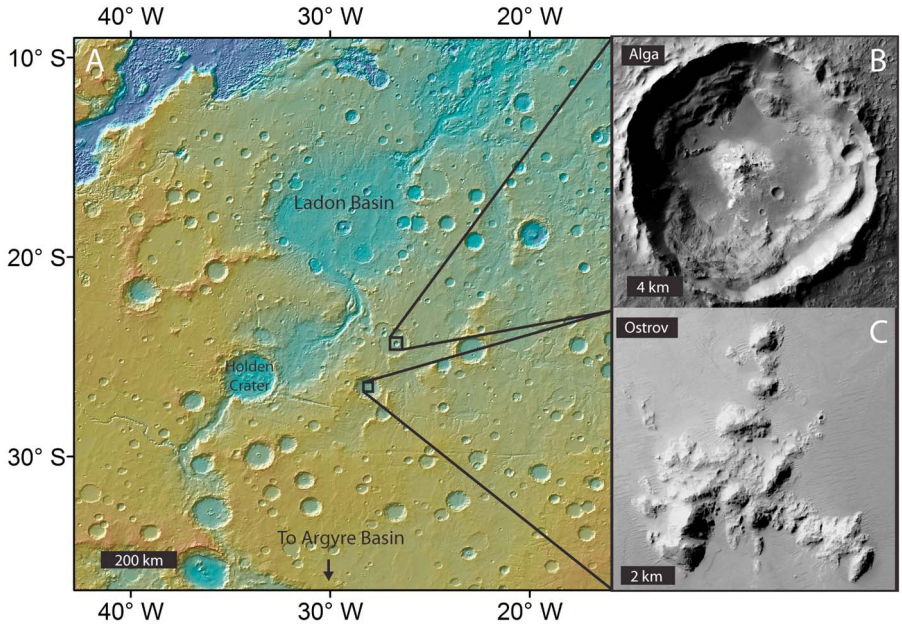

Figure 4. Alga and Ostrov Crater Context Map. (a) Alga and Ostrov craters are located just east of the Margaritifer-Uzboi fluvial system, south of Ladon and east of Holden Crater. (MOLA DEM). (b) Alga is a 18 km crater just off center of the 86 km Chekalin Crater. (CTX: P18_007929_1555_XI_24S026W). (c) Ostrov is a modified 65 km crater (CTX: P17_007639_1514_XN_28S027W).

analysis of the two central peaks. The images were calibrated and atmospherically corrected using the methods described by *Bandfield et al.* [2004]. Spectrally distinct units within each scene were determined by examining CRISM mafic parameters and THEMIS decorrelation stretch (DCS) [*Gillespie et al.*, 1986] images. To quantitatively map the spectral unit distributions, spectra were extracted from distinct units identified in the DCS images and averaged. These spectra were then used to model the scene emissivity with a linear least squares minimization routine. For both Alga and Ostrov, the most olivine-rich spectral units could be modeled as a combination of another unit in the scene plus a laboratory spectrum of olivine. Because of this, the olivine-rich spectral unit does not represent a true end-member and the olivine-rich unit spectrum was replaced with a pure olivine spectrum for mapping the spectral unit distributions [*Rogers and Bandfield*, 2009]. Root-mean square (RMS) error images calculated from the least squares minimization were examined to ensure that all surfaces were relatively well-modeled by the spectral library.

3. Type Region Results

[22] The spectral analysis of CRISM observed unaltered, well-exposed crater central peaks have yielded 23 sites (Table 1). The observed craters range in diameter from ~130 km to 7 km. The observed sites can be divided into four concentrated regions; North Argyre (NA), Northern Hellas (NH), Nili Fossae (NF) and the Northern Plains (NP) (Figure 2 and Table 1) that we will describe to look for regional relationships. While each crater has its own unique attributes, we include in-depth unit analysis of the two best exposed central peaks in Alga and Ostrov Craters (Figure 4) and general descriptions of one example from each designated region to highlight some of the observed diversity and then focus on the aggregate compositions to analyze global trends.

[23] *Alga Crater*. Alga crater is 19 km wide and is located just east of the center of the 85 km diameter degraded Chekalin crater. The rim of Alga crater exposes layered light-toned olivine-bearing outcrops best exposed toward the southeast. The western and northern crater wall and terraces show scattered exposures of olivine- and pyroxene-bearing outcrops. The central peak of Alga is ~200 m high and exposes a complex relationship among local mafic units. The terrain was divided into four units based on morphologic and spectroscopic analysis of the central peak (Figure 5): a distinct light-toned olivine-bearing unit, a pyroxene-bearing bedrock unit, a light-toned pyroxene unit found on the floor of the crater and a fine-grained deposit with a varying clast content that are interpreted to be an impact melt unit on the flanks of the central peak (Figure 6). Representative regions of each unit were analyzed with the methods described above to determine the cation composition and lithology.

[24] *Alga Crater Olivine Unit*. The olivine-bearing unit correlates with partially to well-exposed relatively light-toned massive outcrops and relatively dark deposits bearing abundant light-toned clasts, which drape and appear to flow off the bedrock of the central uplift on the northern slopes. The olivine-rich outcrops are located primarily on the northern and western slopes of the central peak with a few small megablocks observed on the eastern side. This unit typically features a sharp boundary with the adjacent units that are easily observed by the relative contrast in tone, but the unit is also characterized by a dense network of relatively dark-toned fractures and mantles of dark-toned materials, interpreted to be impact melts generated by the Alga-forming event. Spectrally the ratioed olivine exhibits the characteristic olivine absorptions and no other detectable spectral features (Figure 7)

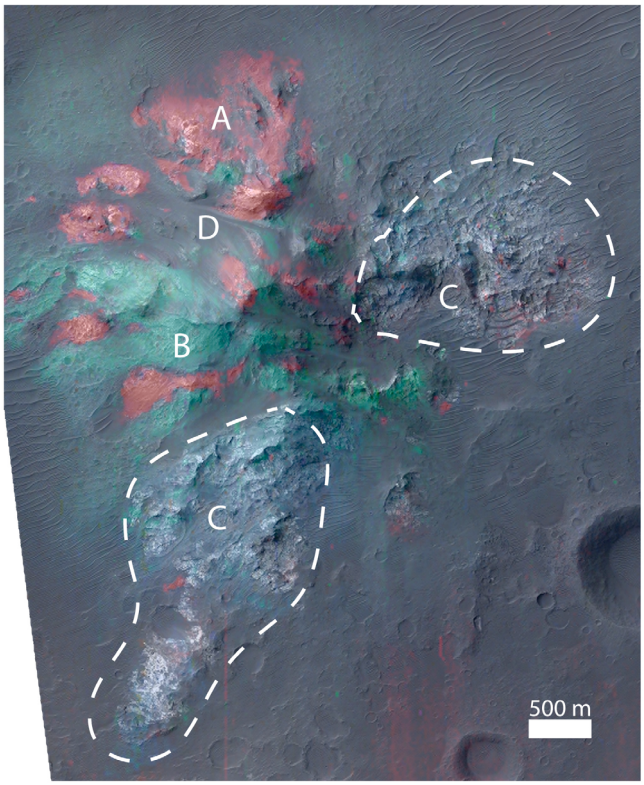

Figure 5. Map of Alga crater central peak units. Olivine-bearing unit (area A). Pyroxene-bearing unit (area B). Light-toned pyroxene (area C). Possible melt unit (area D). CRISM FRT00006415 mafic parameters on HiRISE PSP_007573_1555. R:Olindex2, G:LCPindex, B:HCPindex.

in the VNIR range. Regions of interest were selected from ten locations within the unit for MGM analysis. MGM modeling and composition determination yields modeled result range of $Fo_{9–43}$ with a mean of Fo_{18} (Table 3).

[25] *Alga Crater Pyroxene-Bearing Bedrock Unit*. The pyroxene-bearing bedrock unit comprises the remaining bulk of the central peak bedrock units, dominating the peak's southern portion. Fractures within this unit display a variety of textures ranging from semi-angular on the west side of the peak to tabular fractures on certain parts of the eastern slope of the peak (Figure 6). Spectral analyses of eight regions of interest all confirm low-calcium pyroxene with similar band centers (Figure 8). A slightly longer 2 μm band for the observed 1 μm band position indicates that this unit is relatively Fe-rich [*Adams*, 1974; *Cloutis and Gaffey*, 1991]. NBSR values of each of the pyroxene absorption feature show reassuring agreement between the 1 and 2 μm absorptions (Table 4), supporting the absence of olivine spectral effects, which typically expresses itself as a modification of the 1 μm absorption features. The elevated NBSR values (2 μm: 0.59–0.61) support a LCP enrichment of this pyroxene unit.

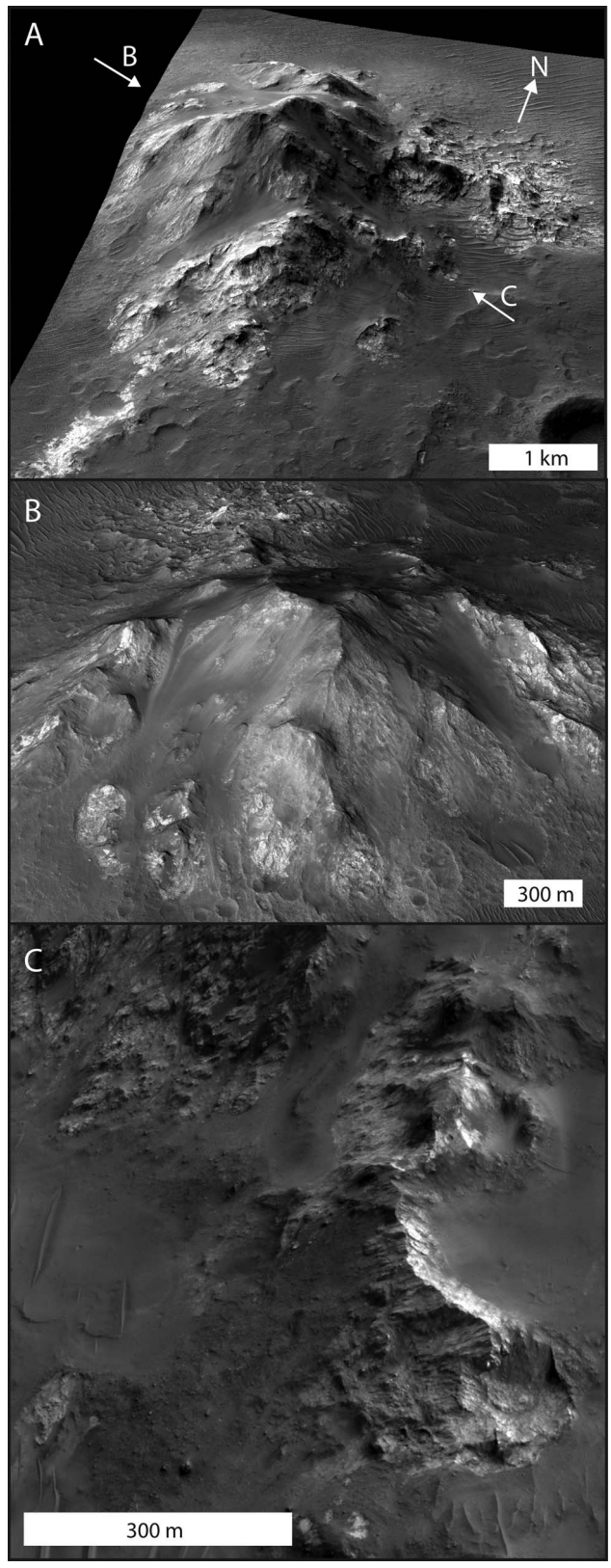

Figure 6. Oblique view of Alga Crater from HiRISE draped on HiRISE DEM (5x vertical exaggeration). (a) View from south showing main peak structure dominated by Pyroxene-bearing bedrock. Light-toned Pyroxene unit seen to south and east of main peak. (b) View of peak from west. Light toned units to left and bottom are Olivine-bearing. Potential melt unit on peak flank following central couloir. (c) View from east showing tabular nature of Pyroxene-bearing bedrock unit.

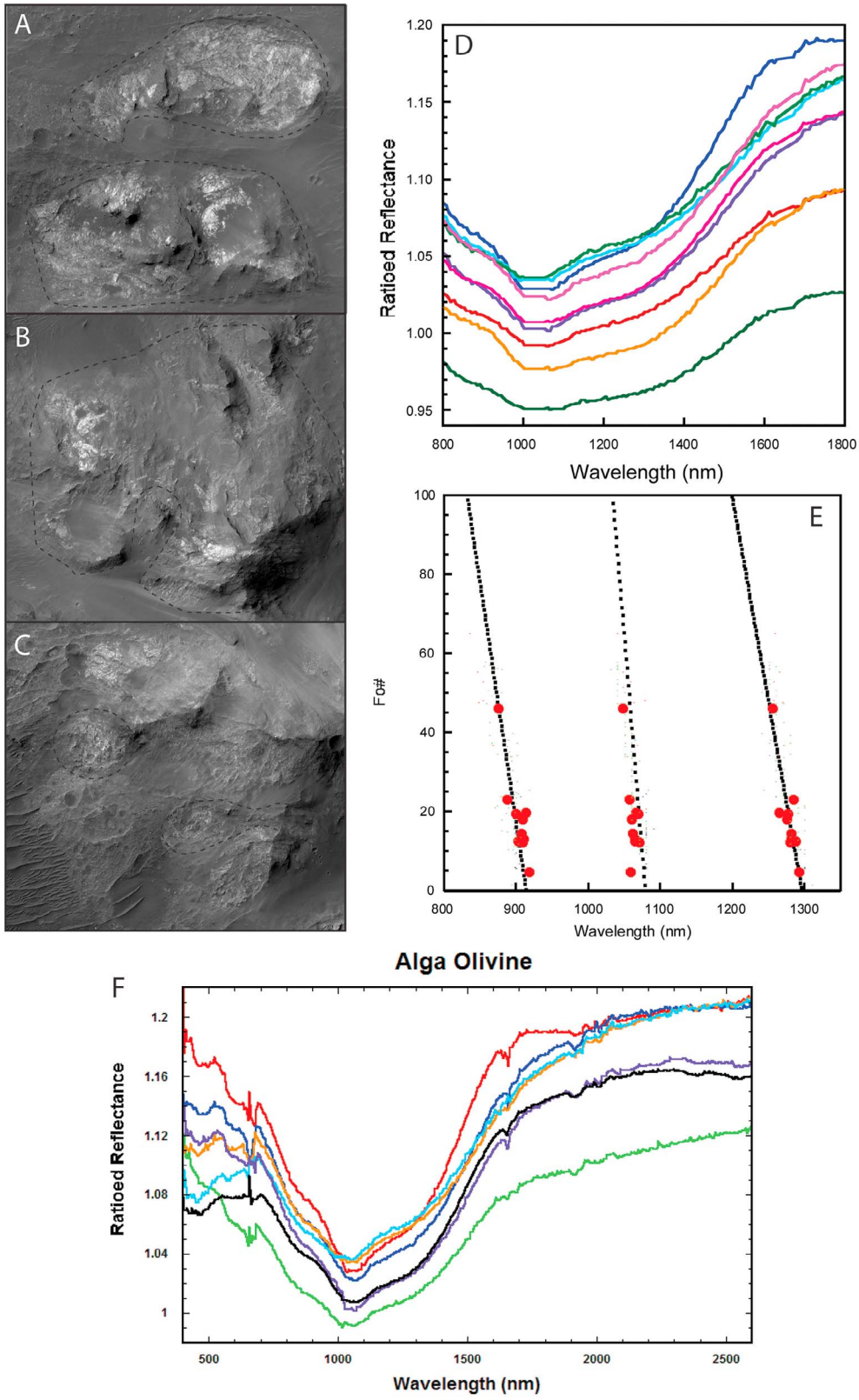

Figure 7. Alga Olivine Results. (a–d) Olivine deposits shown in dotted lines. Truncated spectra used in MGM modeling. (e) MGM modeled olivine band center fits, results in Table 3. (f) Full spectral range of Alga crater olivine.

Table 3. List of Modeled Olivine Regions[a]

	M1–1	M2	M1–2	3-Band Comp (Fo)	Comp Fitting Error	2-Band Comp (Fo)	Comp Difference
North Argyre Olivine Unit							
NA1_1	877	1046	1257	45	160	46	1
NA1_2	899	1072	1282	16	3	15	1
NA1_3	889	1063	1290	18	270	11	7
NA1_4	901	1069	1298	7	172	2	5
NA1_5	902	1069	1293	9	87	6	3
NA1_6	897	1067	1289	14	91	10	3
NA1_7	902	1067	1285	14	43	14	0
NA1_8	900	1079	1281	14	44	13	1
NA1_9	896	1064	1276	22	26	23	1
NA2_1	843	1035	1264	59	1408	44	15
NA2_2	836	1035	1254	68	1172	53	15
NA2_3	838	1031	1251	70	1123	56	13
NA2_4	837	1034	1263	63	1653	45	18
NA4_1	900	1080	1268	20	190	23	3
NA4_2	897	1080	1279	16	86	14	2
NA5_1	835	1040	1258	65	1340	47	18
NA5_2	891	1053	1263	34	135	38	4
NA5_3	874	1048	1247	51	62	53	2
North Hellas Olivine Unit							
NH3_1	895	1074	1294	10	151	4	7
NH3_2	899	1075	1285	13	20	11	2
NH3_3	898	1080	1281	14	82	12	3
NH3_4	899	1080	1281	14	74	12	2
NH4_1	903	1077	1269	20	144	24	4
NH4_2	899	1080	1280	15	71	13	1
NH4_3	899	1081	1279	15	82	13	2
NH4_4	899	1081	1279	15	84	13	1
NH4_5	901	1078	1279	14	47	14	0
NH4_6	897	1088	1276	16	292	13	3
NH4_7	891	1078	1269	25	123	23	2
NH6_1	907	1073	1289	8	5	8	0
NH8_1	888	1065	1252	38	97	42	4
NH8_2	905	1075	1260	24	341	32	8
NH8_3	917	1083	1243	25	1653	43	18
Nili Fossae Olivine Unit							
NF1_1	900	1080	1280	14	67	13	1
NF2_1	904	1075	1293	7	26	4	3
NF2_2	900	1082	1295	5	124	−1	6
NF2_3	899	1080	1280	14	76	13	2
NF2_4	901	1079	1280	14	52	13	1
NF2_5	898	1083	1296	6	183	−1	7
Northern Plains Olivine Unit							
NP1_1	861	1039	1263	51	661	43	8
NP1_2	873	1045	1263	44	285	41	3
NP1_3	887	1055	1266	34	78	35	1
NP1_4	855	1039	1257	57	587	48	8
NP1_5	856	1040	1254	58	466	50	7
NP1_6	867	1044	1246	56	106	56	0
NP1_7	879	1051	1244	50	82	55	5
NP1_8	866	1044	1260	49	355	44	5
NP1_9	870	1041	1252	52	246	52	0
NP1_10	887	1052	1262	36	122	39	3
NP1_11	867	1034	1251	56	436	56	0
NP1_12	883	1050	1261	39	121	41	1
NP1_13	881	1048	1260	41	173	42	1
NP1_14	863	1037	1251	57	360	55	2
NP1_15	866	1039	1248	57	252	56	0
NP1_16	874	1044	1240	56	141	61	5
NP1_17	899	1061	1273	23	78	27	3
NP2_1	900	1068	1286	14	34	12	1
NP2_2	889	1062	1285	21	198	15	5
NP2_3	896	1076	1291	11	114	5	6
NP3_1	874	1059	1298	21	1107	6	16
NP3_2	885	1062	1291	19	419	10	9
NP3_3	905	1071	1282	13	9	15	2
NP3_4	898	1070	1295	9	148	4	6
NP3_5	903	1074	1284	12	1	11	0
NP3_6	898	1074	1287	13	31	10	3
NP3_7	899	1079	1283	13	57	11	3
NP3_8	895	1077	1292	10	142	4	7
NP3_9	871	1061	1301	21	1378	3	18
NP3_10	888	1069	1303	10	607	−2	12
NP4_1	874	1051	1278	34	511	26	8
NP4_2	862	1049	1279	39	953	25	14
NP4_3	858	1043	1270	47	861	36	12
NP4_4	863	1047	1273	43	709	32	11
NP4_5	886	1064	1263	33	1	33	0
NP4_6	871	1047	1258	47	181	45	3
NP4_7	887	1074	1293	15	337	4	10
NP5_1	896	1063	1272	24	23	26	2
NP5_2	892	1058	1269	29	73	31	2
NP5_3	888	1062	1268	30	9	30	1
NP5_4	870	1043	1250	53	164	53	0
NP5_5	901	1065	1249	34	441	45	11
NP5_6	894	1067	1256	33	139	38	6
NP5_7	894	1055	1260	34	150	40	6
NP5_8	897	1080	1279	16	93	14	2
NP5_9	896	1061	1262	30	82	35	5
NP5_10	901	1069	1270	21	53	25	4
NP5_11	899	1079	1280	15	56	13	2
NP5_12	898	1080	1280	15	81	13	2
NP5_13	901	1063	1262	28	187	35	8
NP5_14	898	1071	1276	19	2	20	1
NP5_15	898	1076	1277	17	34	17	1
NP5_16	896	1064	1243	40	435	50	11
NP5_17	879	1043	1237	56	253	64	8
NP5_18	901	1058	1246	37	547	50	13
NP5_19	890	1055	1261	35	90	39	4
NP5_20	899	1065	1268	25	64	29	5
NP5_21	904	1064	1265	24	169	32	7
NP6_1	857	1049	1290	36	1770	17	19
NP6_2	878	1076	1314	7	1478	−14	21
NP6_3	864	1058	1299	26	1691	5	20
NP6_4	873	1065	1308	15	1512	−5	20

[a]Bandcenters and Compositions. Column 1:Region ID Region: Region#: ROI #, 2: Olivine M1–1 band, 3: Olivine M2 band, 4:Olivine M1–2 band, 5: Olivine least squares fit composition calculated from M1–1, M2, and M1–2 bands, 6: Least squares fitting error for three band fit, 7: Olivine least squares fit composition for M2 and M1–2 bands, 8: Absolute difference between 3 band and 2 band compositions.

[26] *Alga Crater Light-Toned Pyroxene Unit.* The second pyroxene-bearing unit is located on the crater floor in two distinct occurrences just south and east of the central peak (Figure 9). This unit is lighter than the pyroxene-bearing bedrock and is significantly brecciated with a wide range of clast sizes. The lighter-tone of the bedrock makes this unit easy to detect and distinguish from the darker background material of the crater floor. MGM spectral analysis of 7 regions show well-formed pyroxene spectral features with band centers similar to the pyroxene bedrock unit, again consistent with a relatively high-Fe, low calcium pyroxene. However, this unit displays less VNIR spectral contrast, creating more error in the spectral modeling. The lower spectral contrast may be caused by several contributing factors, the most likely being smaller grain sizes or the intimate mixing of a spectrally neutral but relativity high albedo material. Both of these options would lead to the albedo

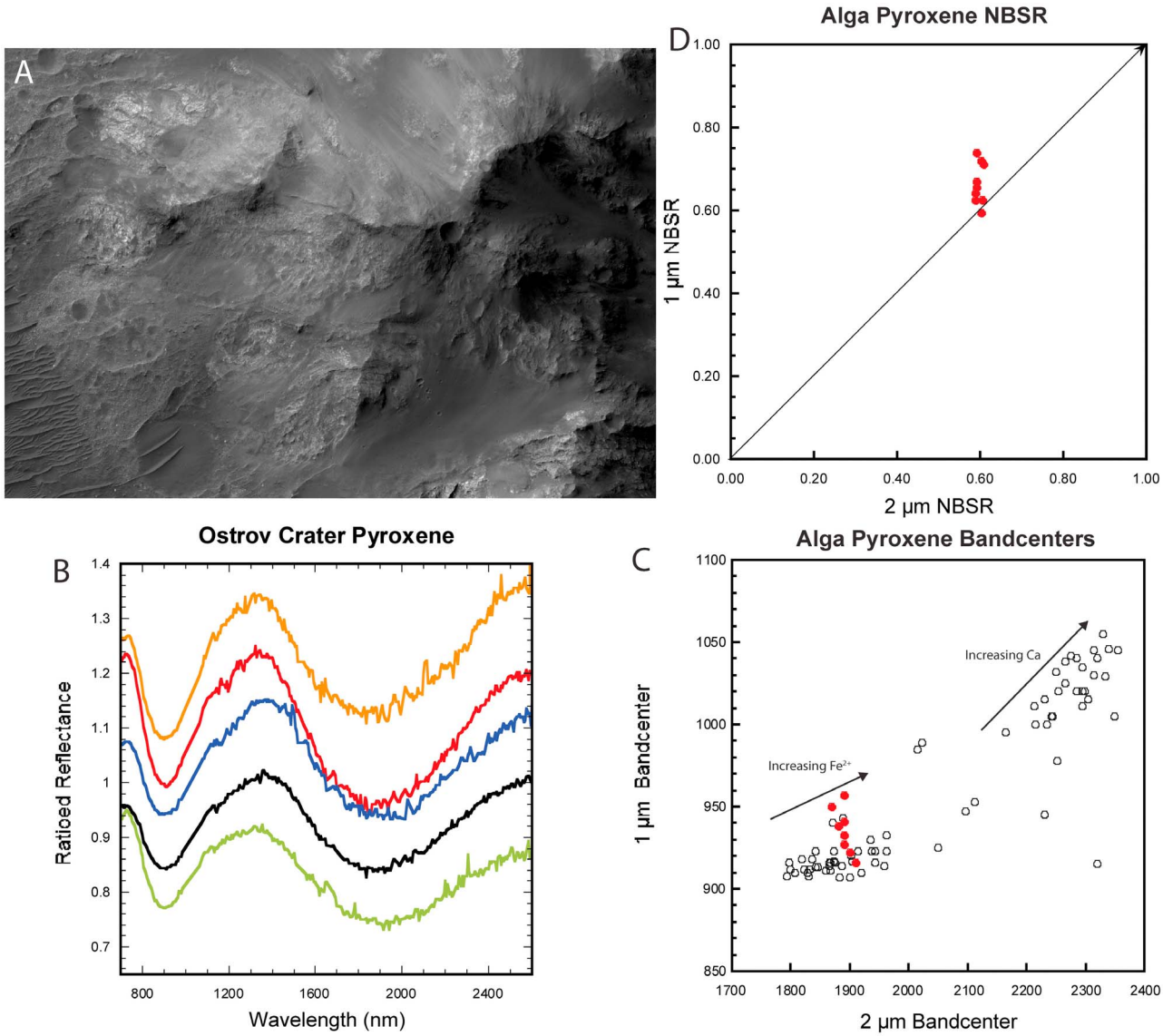

Figure 8. Alga pyroxene results. (a) Southwest portion of Alga central peak containing most of the Pyroxene Bedrock Unit. (b) Ratioed Alga pyroxene spectra used in MGM analysis. (c) Alga crater Pyroxene Bedrock 1-, 2 μm band centers plotted against terrestrial pyroxene band centers [*Adams*, 1974; *Cloutis and Gaffey*, 1991]. From bottom left to upper right, pyroxene composition goes from Mg-rich to Fe-rich to Ca-rich. Alga pyroxene plot as low-Ca, moderate-Fe. (d) Pyroxene NBSR demonstrating a consistent LCP enrichment.

contrast and observed spectral properties, but the rocky appearance of the outcrop would support the mixing hypothesis with a material similar to the glassy melt unit described below.

[27] Three of the regions of interest (ROI: 1, 2, 5) display a secondary absorption feature centered at 2.2 μm superimposed on the pyroxene absorption (Figure 10). This absorption is similar in width and position to a metal-OH feature, particularly Si-OH [*Anderson and Wickersheim*, 1964]. These spectral features may indicate that this unit is a mixture of pyroxene and a silica-rich impact melt or potentially a product of an impact induced hydrothermal activity. The presence of these features in only a few of the examined regions may be due to a heterogeneous molecular hydration throughout this unit. This feature is unique to this unit and not observed in any other pyroxene unit examined in this study.

[28] *Alga Crater Impact Melt.* The final unit that figures prominently in the central peak is a fine-grained deposit that displays weak pyroxene features and makes up a large part of the western portion of the central peak (Figure 11). This unit is characterized by potential flow textures going downslope and contains meter-sized clasts of the pyroxene-bearing bedrock at low elevations. Based on these characteristics and geologic context we interpret this unit as an impact melt-bearing deposit. The melt is located on the central peak apex and fills the peak's northern, southern and eastern couloirs.

Table 4. Pyroxene Observation Table[a]

	1 μm LCP Band Center	1 μm LCP Band Depth	1 μm HCP Band Center	1 μm HCP Band Depth	1 μm NBSR	2 μm LCP Band Center	2 μm LCP Band Depth	2 μm HCP Band Center	2 μm HCP Band Depth	2 μm NBSR	1 μm Band Center	2 μm Band Center
North Argyre Pyroxene												
NA1_1	889	−0.11	1075	−0.05	0.67	1760	−0.12	2145	−0.08	0.59	933	1893
NA1_2	886	−0.12	1064	−0.07	0.63	1746	−0.14	2138	−0.10	0.59	938	1884
NA1_3	893	−0.09	1075	−0.05	0.66	1757	−0.10	2152	−0.07	0.59	941	1892
NA1_4	890	−0.11	1075	−0.06	0.64	1751	−0.13	2133	−0.09	0.59	941	1886
NA1_5	889	−0.10	1078	−0.04	0.72	1773	−0.12	2135	−0.08	0.60	922	1896
NA1_6	896	−0.08	1068	−0.06	0.59	1759	−0.14	2131	−0.09	0.60	957	1890
NA1_7	892	−0.10	1080	−0.04	0.71	1769	−0.12	2132	−0.08	0.61	927	1891
NA1_8	893	−0.08	1065	−0.03	0.74	1782	−0.10	2148	−0.07	0.59	916	1909
NA1_9	894	−0.11	1082	−0.06	0.63	1743	−0.13	2129	−0.08	0.61	950	1867
NA2_1	901	−0.23	1099	−0.06	0.79	1801	−0.21	2142	−0.11	0.65	918	1892
NA2_2	899	−0.16	1086	−0.05	0.76	1850	−0.17	2199	−0.08	0.68	898	1912
NA2_3	902	−0.15	1110	−0.05	0.74	1912	−0.26	2528	−0.16	0.62	827	1892
NA2_4	903	−0.16	1103	−0.04	0.80	1839	−0.17	2183	−0.07	0.70	911	1904
NA2_5	896	−0.20	1083	−0.05	0.80	1841	−0.16	2162	−0.07	0.71	916	1911
NA2_6	898	−0.20	1078	−0.07	0.74	1775	−0.19	2168	−0.11	0.63	919	1877
NA2_7	901	−0.10	1151	−0.04	0.71	1936	−0.22	2517	−0.18	0.56	916	2141
NA2_8	891	−0.22	1078	−0.03	0.86	1834	−0.16	2142	−0.05	0.77	902	1887
NA2_9	920	−0.15	1077	−0.02	0.88	1894	−0.12	2299	0.00	1.00	981	1979
NA2_10	900	−0.15	1141	−0.02	0.89	1908	−0.25	2563	−0.21	0.54	805	1875
NA3_1	905	−0.02	1082	0.00	0.84	1779	−0.06	2164	−0.03	0.64	921	1882
NA4_1	920	−0.08	1075	−0.03	0.70	1809	−0.09	2200	−0.07	0.56	957	1954
NA4_2	913	−0.07	1084	−0.03	0.67	1792	−0.07	2192	−0.06	0.56	961	1941
NA4_3	906	−0.06	1088	−0.05	0.54	1783	−0.08	2181	−0.07	0.56	997	1932
NA6_1	904	−0.02	1080	−0.03	0.46	1872	−0.04	2285	−0.03	0.58	994	1991
NA6_2	921	−0.02	1074	−0.03	0.46	1850	−0.05	2236	−0.03	0.61	1005	1964
NA6_3	919	−0.02	1075	−0.02	0.47	1850	−0.04	2232	−0.03	0.59	1005	1987
NA6_4	923	−0.06	1120	−0.07	0.49	1744	−0.10	2165	−0.07	0.59	999	1876
NA6_5	916	−0.05	1112	−0.05	0.50	1762	−0.08	2158	−0.06	0.60	990	1890
NA6_6	899	−0.02	1081	−0.02	0.41	1906	−0.03	2340	−0.04	0.47	994	2100
NA6_7	920	−0.05	1115	−0.05	0.51	1792	−0.07	2180	−0.04	0.62	994	1901
NA6_8	906	−0.07	1105	−0.09	0.46	1735	−0.13	2150	−0.10	0.57	1021	1919
NA6_9	915	−0.03	1088	−0.04	0.47	1749	−0.07	2155	−0.05	0.57	1001	1892
North Hellas Pyroxene												
NH1_1	957	−0.07	1183	−0.06	0.54	1761	−0.10	2222	−0.08	0.57	1014	1939
NH1_2	948	−0.07	1192	−0.09	0.44	1749	−0.11	2177	−0.07	0.61	1098	1955
NH1_3	930	−0.05	1109	−0.07	0.42	1756	−0.11	2193	−0.10	0.52	1016	1955
NH1_4	921	−0.01	1060	−0.02	0.35	1837	−0.06	2208	−0.04	0.59	1010	1957
NH2_1	920	−0.08	1075	−0.03	0.70	1809	−0.09	2200	−0.07	0.56	957	1954
NH2_2	913	−0.07	1084	−0.03	0.67	1792	−0.07	2192	−0.06	0.56	961	1941
NH2_3	906	−0.06	1088	−0.05	0.54	1783	−0.08	2181	−0.07	0.56	997	1932
NH3_1	918	−0.04	1073	−0.03	0.54	1827	−0.08	2216	−0.07	0.54	983	1984
NH3_2	905	−0.05	1082	−0.05	0.54	1800	−0.11	2180	−0.09	0.56	986	1952
NH3_3	900	−0.06	1085	−0.05	0.57	1782	−0.10	2165	−0.08	0.56	978	1935
NH3_4	909	−0.06	1083	−0.05	0.56	1803	−0.11	2184	−0.08	0.56	983	1953
NH3_5	907	−0.06	1083	−0.05	0.55	1796	−0.11	2192	−0.09	0.54	989	1958
NH3_6	907	−0.01	1084	−0.02	0.38	1811	−0.03	2239	−0.02	0.58	1015	1977
NH3_7	906	−0.02	1079	−0.04	0.40	1804	−0.07	2215	−0.06	0.56	1025	1950
NH3_8	894	−0.03	1086	−0.03	0.47	1845	−0.09	2242	−0.07	0.56	989	1984
NH3_9	898	−0.02	1060	−0.02	0.54	1859	−0.07	2235	−0.06	0.55	965	2004
NH3_10	905	−0.06	1085	−0.05	0.53	1793	−0.10	2182	−0.08	0.56	991	1945
NH3_11	900	−0.07	1080	−0.06	0.52	1781	−0.09	2180	−0.08	0.55	991	1941
NH3_12	895	−0.06	1081	−0.05	0.54	1784	−0.09	2183	−0.08	0.55	980	1945
NH3_13	913	−0.03	1083	−0.01	0.71	1869	−0.06	2246	−0.05	0.55	932	2008
NH3_14	910	−0.03	1069	−0.01	0.68	1879	−0.05	2255	−0.04	0.56	935	2013
NH3_15	901	−0.06	1084	−0.05	0.53	1782	−0.10	2176	−0.08	0.56	988	1933
NH4_1	912	−0.04	1080	−0.04	0.52	1814	−0.06	2219	−0.04	0.60	993	1927
NH4_2	904	−0.06	1097	−0.05	0.51	1784	−0.06	2199	−0.04	0.61	978	1893
NH4_3	893	−0.05	1089	−0.05	0.51	1784	−0.08	2195	−0.05	0.62	994	1892
NH4_4	925	−0.05	1069	−0.02	0.70	1868	−0.08	2219	−0.06	0.60	956	1982
NH4_5	777	−0.07	1023	−0.07	0.47	1813	−0.09	2256	−0.07	0.55	955	1997
NH4_6	854	−0.08	1203	−0.06	0.57	1961	−0.11	2467	−0.04	0.74	957	1984
NH4_7	901	−0.01	1082	−0.01	0.57	1859	−0.03	2283	−0.02	0.56	847	1993
NH5_1	922	−0.07	1128	−0.04	0.64	1851	−0.08	2190	−0.03	0.71	960	1917
NH5_2	921	−0.06	1121	−0.03	0.64	1844	−0.06	2192	−0.03	0.69	960	1919
NH5_3	917	−0.06	1101	−0.03	0.69	1861	−0.06	2180	−0.03	0.69	952	1937
NH5_4	903	−0.02	1079	−0.02	0.56	1900	−0.03	2301	0.00	0.86	992	1961
NH5_5	911	−0.04	1080	−0.01	0.73	1866	−0.04	2275	−0.02	0.71	937	1924

Table 4. (continued)

	1 μm LCP Band Center	1 μm LCP Band Depth	1 μm HCP Band Center	1 μm HCP Band Depth	1 μm NBSR	2 μm LCP Band Center	2 μm LCP Band Depth	2 μm HCP Band Center	2 μm HCP Band Depth	2 μm NBSR	1 μm Band Center	2 μm Band Center
NH5_6	921	−0.07	1129	−0.05	0.56	1809	−0.06	2183	−0.05	0.58	982	1936
NH5_7	915	−0.04	1088	−0.05	0.47	1811	−0.07	2191	−0.05	0.56	996	1956
NH5_8	920	−0.04	1095	−0.03	0.62	1896	−0.05	2236	−0.02	0.75	967	1950
NH5_9	923	−0.05	1104	−0.03	0.61	1850	−0.04	2207	−0.02	0.65	976	1947
NH6_1	900	−0.03	1087	−0.03	0.48	1872	−0.02	2291	−0.01	0.73	970	2011
NH7_1	901	−0.01	1080	−0.01	0.60	1900	−0.04	2300	−0.02	0.66	971	1977
NH8_1	910	−0.05	1086	−0.03	0.60	1937	−0.03	2279	−0.02	0.60	937	2010
NH8_2	873	−0.04	1075	−0.04	0.49	1949	−0.03	2329	−0.04	0.46	996	2171
NH9_1	853	−0.08	1010	−0.09	0.47	1753	−0.24	2224	−0.19	0.56	923	1335
NH9_2	857	−0.08	1062	−0.03	0.70	1817	−0.13	2344	−0.11	0.56	882	1341
NH9_3	923	−0.08	1022	−0.03	0.75	1724	−0.14	2159	−0.11	0.55	938	1340
NH9_4	912	−0.09	1031	−0.05	0.62	1812	−0.15	2274	−0.12	0.55	952	1335
						Nili Fossae Pyroxene						
NF1_1	854	−0.08	1019	−0.05	0.61	1750	−0.11	2104	−0.08	0.57	894	1886
NF1_2	891	−0.06	1064	−0.04	0.61	1755	−0.09	2121	−0.06	0.58	947	1897
NF1_3	795	−0.07	1038	−0.06	0.54	1787	−0.09	2304	−0.06	0.63	866	1886
NF1_4	856	−0.08	1044	−0.06	0.56	1769	−0.09	2190	−0.07	0.58	928	1922
NF1_5	896	−0.09	1095	−0.04	0.69	1754	−0.09	2168	−0.07	0.56	943	1920
NF1_6	879	−0.08	1071	−0.05	0.62	1769	−0.10	2166	−0.07	0.58	948	1918
NF2_1	922	−0.03	1110	−0.04	0.42	1794	−0.06	2229	−0.04	0.60	1063	1898
NF2_2	922	−0.08	1141	−0.07	0.52	1734	−0.10	2137	−0.07	0.60	1039	1818
NF2_3	909	−0.04	1078	−0.03	0.59	1781	−0.07	2179	−0.06	0.56	969	1934
NF2_4	920	−0.03	1064	−0.02	0.56	1771	−0.06	2194	−0.05	0.57	969	1911
NF2_5	940	−0.07	1168	−0.09	0.44	1769	−0.09	2203	−0.06	0.61	1156	1828
NF2_6	906	−0.03	1097	−0.04	0.43	1816	−0.04	2236	−0.03	0.62	1045	1946
						Northern Plains Pyroxene						
NP1_1	918	−0.04	1118	−0.05	0.46	1762	−0.06	2192	−0.04	0.59	1012	1880
NP1_2	917	−0.06	1131	−0.06	0.48	1736	−0.08	2173	−0.06	0.59	1017	1882
NP1_3	911	−0.02	1075	−0.04	0.40	1789	−0.06	2201	−0.05	0.55	1012	1946
NP1_4	920	−0.02	1063	−0.02	0.48	1814	−0.06	2201	−0.04	0.58	988	1945
NP1_5	913	−0.02	1083	−0.03	0.41	1767	−0.05	2206	−0.04	0.59	1017	1882
NP1_6	907	−0.01	1087	−0.02	0.36	1774	−0.04	2215	−0.03	0.62	1032	1878
NP1_7	913	−0.03	1103	−0.05	0.37	1745	−0.09	2170	−0.06	0.60	1035	1876
NP1_8	913	−0.02	1084	−0.04	0.38	1786	−0.07	2181	−0.05	0.58	1026	1921
NP1_9	911	−0.02	1091	−0.03	0.42	1782	−0.06	2176	−0.04	0.57	1020	1923
NP2_1	877	−0.10	1068	−0.11	0.48	1939	−0.06	2302	−0.11	0.36	967	2194
NP2_2	900	−0.04	1079	−0.03	0.53	1904	−0.05	2279	−0.06	0.42	972	2141
NP2_3	908	−0.04	1076	−0.05	0.46	1901	−0.07	2318	−0.12	0.37	984	2208
NP2_4	874	−0.08	1084	−0.09	0.46	2004	−0.06	2377	−0.13	0.34	958	2287
NP2_5	906	−0.03	1077	−0.02	0.59	1897	−0.03	2321	−0.08	0.29	920	2267
NP5_1	918	−0.04	1118	−0.05	0.46	1762	−0.06	2192	−0.04	0.59	1012	1880
NP5_2	917	−0.06	1131	−0.06	0.48	1736	−0.08	2173	−0.06	0.59	1017	1882
NP5_3	911	−0.02	1075	−0.04	0.40	1789	−0.06	2201	−0.05	0.55	1012	1946
NP5_4	920	−0.02	1063	−0.02	0.48	1814	−0.06	2201	−0.04	0.58	988	1945
NP5_5	913	−0.02	1083	−0.03	0.41	1767	−0.05	2206	−0.04	0.59	1017	1882
NP5_6	907	−0.01	1087	−0.02	0.36	1774	−0.04	2215	−0.03	0.62	1032	1878
NP5_7	913	−0.03	1103	−0.05	0.37	1745	−0.09	2170	−0.06	0.60	1035	1876
NP5_8	913	−0.02	1084	−0.04	0.38	1786	−0.07	2181	−0.05	0.58	1026	1921
NP5_9	911	−0.02	1091	−0.03	0.42	1782	−0.06	2176	−0.04	0.57	1020	1923
NP5_10	920	−0.03	1112	−0.04	0.48	1758	−0.07	2160	−0.05	0.59	1012	1886
NP5_11	914	−0.03	1097	−0.04	0.43	1756	−0.07	2167	−0.05	0.61	1017	1877
NP5_12	909	−0.01	1073	−0.01	0.53	1824	−0.06	2241	−0.05	0.55	980	1969
NP5_13	902	−0.01	1079	−0.01	0.52	1899	−0.03	2301	−0.02	0.53	987	2052
NP5_14	905	−0.11	1097	−0.08	0.56	1745	−0.16	2142	−0.12	0.57	940	1907
NP5_15	917	−0.06	1088	−0.05	0.53	1807	−0.12	2206	−0.10	0.55	1002	1969
NP5_16	912	−0.03	1082	−0.02	0.60	1784	−0.06	2184	−0.04	0.57	967	1922

[a]MGM fits of pyroxene spectra. LCP and HCP bandcenters and NBSR were determined by 5 Gaussian modeling. NBSR is calculated from bandstrengths (LCP/(LCP + HCP). One and 2 μm bandcenters determined by 3 Gaussian modeling.

The high elevation regions of this unit near the peak summit appear clast free at HiRISE's 25 cm/pixel resolution. Near the base of the peak the melt contains meter sized clasts of the pyroxene-bearing material. All examined regions of the melt unit on the central peak show detectable pyroxene spectral signatures. This unit has similar band centers to the other pyroxene units but with much weaker band depths.

[29] *Pyroxene Unit Comparison*. The Pyroxene Bedrock, Light-Toned Pyroxene, and Impact Melt units all display clear pyroxene spectral absorptions with similar band centers

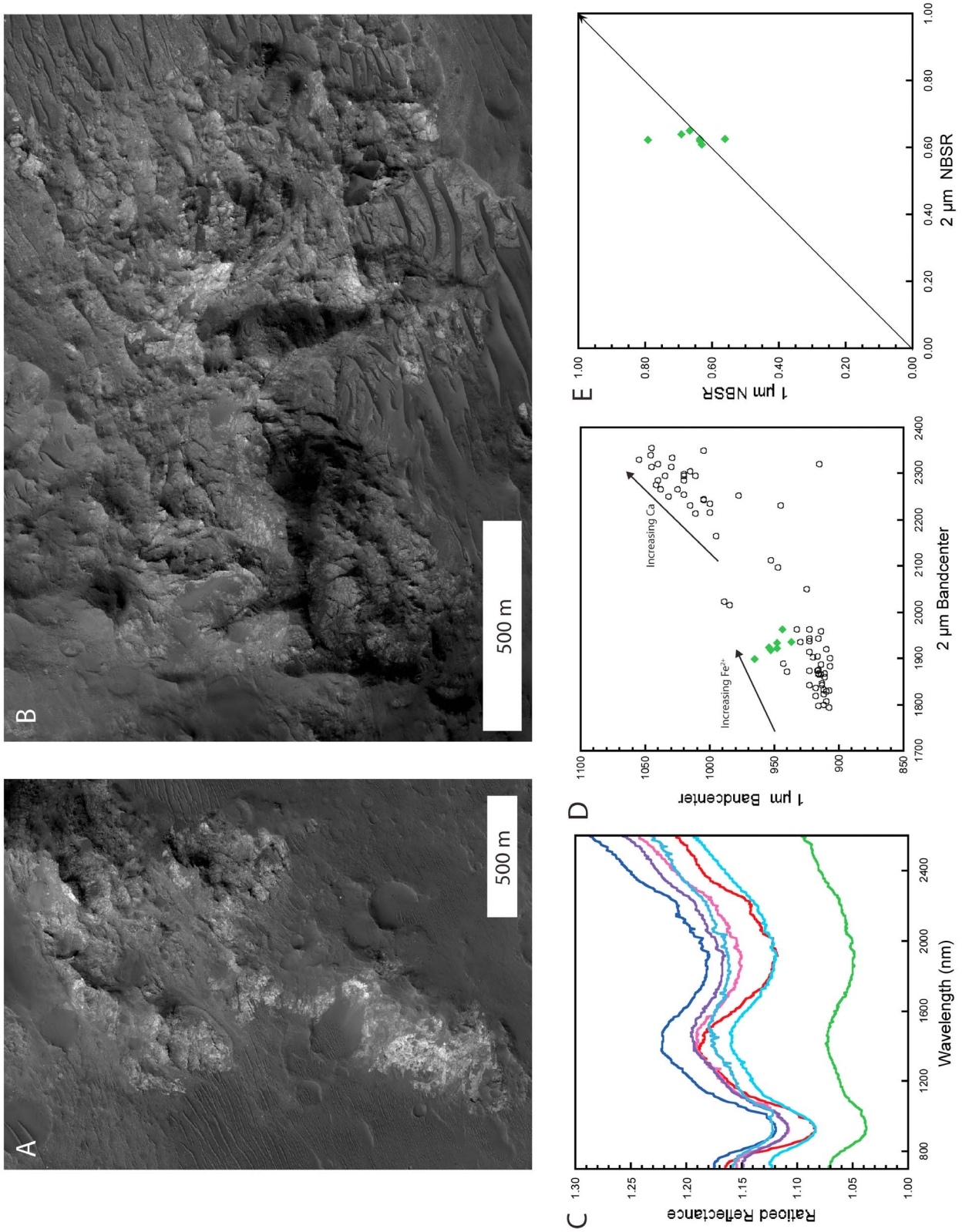
A
500 m
B
500 m
C
Ratioed Reflectance
Wavelength (nm)
D
1 µm Bandcenter
2 µm Bandcenter
Increasing Ca
Increasing Fe2+
E
1 µm NBSR
2 µm NBSR

Figure 9

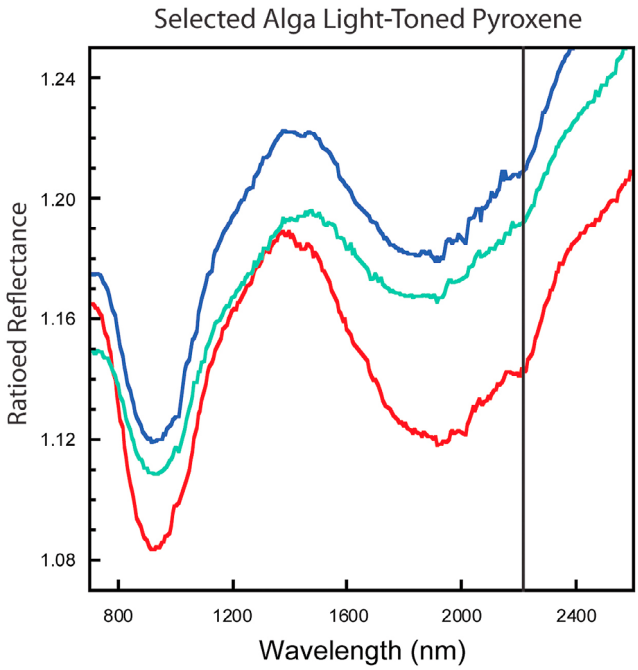

Figure 10. Selected Light-toned Pyroxene Spectra (ROI: 1, 2, 5). Spectra highlights 2.2 μm feature consistent with Si-OH feature with line at 2.2 μm. Potentially the result of hydration of a silica rich impact melt or an impact induced hydrothermal system.

but have a significant difference in band depth (Figure 12). The Pyroxene Bedrock has a low calcium signature with a well-developed 1.2 μm shoulder caused by Fe^{2+} in the M1 site [*Klima et al.*, 2008]. Strong spectral absorptions make this unit the best developed pyroxene member in the scene. Conversely, the impact melt unit has a weak pyroxene band depth and is thought to be comprised of an intimate mixture of spectrally neutral glass with clasts of the pyroxene units providing the relatively weak spectral absorptions. The remaining Light-Toned Pyroxene unit has an intermediate band depth but similar band positions as the Pyroxene Bedrock signifying similar composition but with the possible addition of a brightening spectrally neutral component. Under this model, the three pyroxene units are accessing the same lithologic material but are including varying degrees of spectrally neutral materials. The Impact Melt unit would have a quenched glass component to the matrix that would provide the spectral modification, while the modifying material in the Light-Toned Unit is less clear. Impact glass produced in this impact is a possibility as is melt from the preexisting Chekalin crater or other nearby crater basins, but also melt can be injected into fractures during uplift formation. Alternative materials such as plagioclase and quartz could also provide the desired spectral effect but are difficult to constrain with current observations. An alternate possibility is that shock effects on pyroxene can affect spectral contrast, but not the bandcenters [*Adams*, 1979].

[30] *Ostrov Crater*. The nearby Ostrov crater provides another well exposed central peak to apply the MGM compositional analysis. Ostrov is a 65 km diameter crater located 150 km to the southwest of Alga. Ostrov has had significantly more modification from erosional modification and deposition than Alga, exemplified by a deeply dissected rim and multiple fans filling the crater interior. The central peak structure stands above these deposits and display strong mafic absorption features (Figure 13a). While Ostrov displays several important similarities with Alga, it is simplified with only three discernible spectral units; an olivine-bearing and a pyroxene-bearing unit and a third spectrally bland region that may be analogous to the glassy melt unit. Much like what we observe in Alga, these units are strongly dominated by a specific mineral phase with little evidence of spectral mafic mixing.

[31] *Ostrov Crater Olivine Unit*. The olivine-bearing unit in Ostrov (Figure 13) is characterized by the inclusion of many small light-toned outcrops with the olivine dominated region but otherwise is morphologically similar to the pyroxene-bearing unit. The unit has a very sharp boundary with the pyroxene-bearing units and shows no spectral signature of a pyroxene component, again indicating a minimal pyroxene component. A spectral feature near 0.9 μm affects the fit of the M1 absorption in each of the ratioed spectra, requiring the use of the M2 and M1–2 bands for determining the cation composition. The MGM analysis of four regions of interest within the olivine unit result in slightly elevated Fo# compared to the Alga olivine unit. The measured olivine spectra had atypical response in the S-detector data. This response is unsuitable for full MGM modeling due to distortion of the M1–1 spectral band. The long wavelength shoulder of the olivine spectra is well formed and suitable for modeling, making the calculation of the Fo# that was done with only the M2 and M1–2 absorptions more reliable for this unit. The high-quality of the near-infrared data and well-developed olivine absorption in this region makes the modeled fit reliable even with the two bands. The longest wavelength M1–2 absorption is the best constrained by the spectra and least dependent on small band center shifts. This unit displays values ranging Fo_{44} to Fo_{56} with a mean of Fo_{50}.

[32] *Ostrov Crater Pyroxene Unit*. The Ostrov crater pyroxene unit spatially dominates the central peak structure. Nine regions of interest have been selected for MGM processing based the extent of pyroxene exposure. The resulting band center determination is consistent with a very low Ca, moderate Fe pyroxene (Figure 14). NBSR values of these pyroxenes show close agreement between the 1 and 2 μm values, supporting a relatively pure pyroxene composition. NBSR values fall in the rage from 0.6 to 0.8, indicating enrichment in LCP.

Figure 9. Alga Light-toned pyroxene results. (a) HiRISE view of southern Light-toned Pyroxene Unit. (b) HiRISE view of eastern Light-toned Pyroxene Unit. (c) Ratioed Alga Light-toned Pyroxene spectra used in MGM analysis. (d) Alga crater Light-toned Pyroxene 1-, 2 μm band centers plotted against terrestrial pyroxene band centers [*Adams*, 1974; *Cloutis and Gaffey*, 1991]. From bottom left to top right, pyroxene composition goes from Mg-rich to Fe-rich to Ca-rich. Alga Light-toned pyroxene plot as low-Ca, moderate to high Fe. (e) Pyroxene NBSR demonstrating a consistent LCP enrichment. Values listed in Table 4.

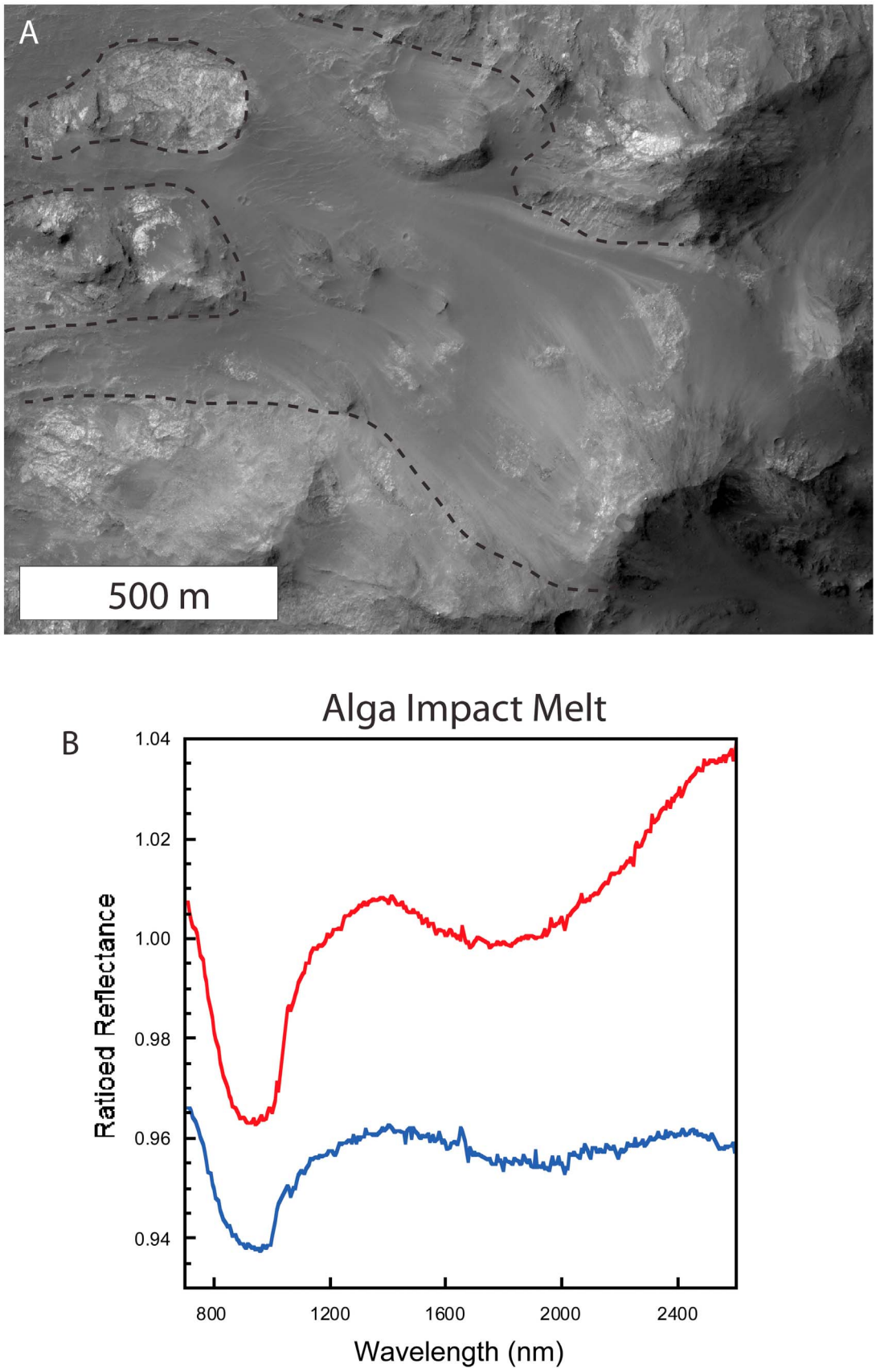

Figure 11. Impact melt. (a) HiRISE view of northern section of Alga central peak with impact melt unit centered in dotted line. (b) Ratioed Alga impact melt spectra.

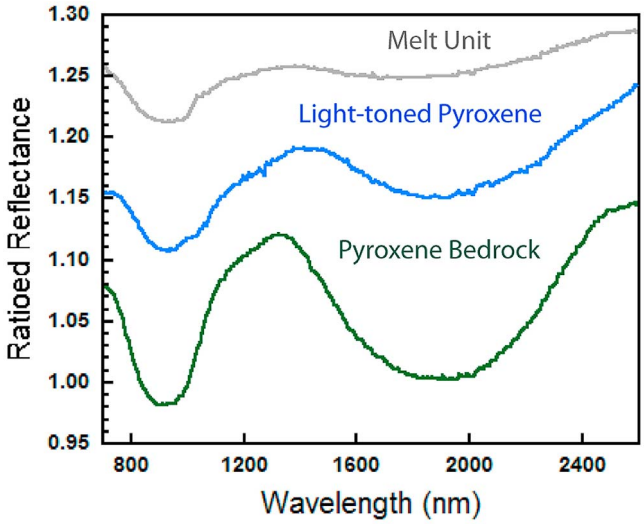

Figure 12. Pyroxene comparison. Here we plot representative spectral from the pyroxene bedrock, light-toned pyroxene, and impact melt units. We see that the band centers are similar but a strong difference in absorption strength. We suggest that all three units are sampling the same composition units but are distinguished by differing quantities of a post-impact spectrally modifying component such as an impact glass.

Compared to the Alga pyroxene these are even more enriched in LCP and have slightly less Fe content (Table 4).

[33] *THEMIS Spectral Analysis*. Analysis of THEMIS observations of Alga's central peak identifies three main spectral units (Figure 15). The first type is dominated by olivine, but is not a spectral match to pure olivine. The THEMIS spectrum is consistent with olivine plus one or more components; a good spectral match can be achieved with a 60:40 mixture of olivine and a palagonite-like high-silica poorly crystalline phase. It can also be well modeled as a mixture of olivine plus the surrounding central peak surface. The second spectral type maps to the majority of central peak and is spectrally consistent with TES Surface Type 1 [*Bandfield et al.*, 2000], within the THEMIS spectral range, though the spectral bands of THEMIS limit the determination of a precise mineralogy. The third type is spectrally similar to an intermediate between Surface Type 1 and Surface Type 2 [*Bandfield et al.*, 2000] and maps to the crater floor and rim. Surface Type 1 is considered to be basaltic in nature. Surface Type 2 is consistent with altered basalt [*Wyatt and McSween*, 2002] or some elevated silica content and may represent the mixture of the central peak mafics with a glassy impact melt component.

[34] THEMIS analysis of Ostrov central peak (Figure 15) can distinguish three spectra units. The first maps to the CRISM olivine-bearing units and is dominated by olivine, but is not a spectral match to pure olivine, similar to the Alga olivine unit. The second type maps to the pyroxene-bearing units and is spectrally consistent with high concentrations of LCP; however the coarse resolution prohibits precise and unique mineralogic assignments. The third type has low emissivity in shorter wavelengths (~8.5–9.5 μm) and higher emissivity in longer wavelengths (11–12 μm), consistent with a low abundance of mafic minerals.

4. Regional Analysis

[35] *North Argyre*. The Northern Argyre (NA) region has contains six central peaks in this study that have well-defined, unaltered mafic spectra, including Alga Crater (NA1) and Ostrov Crater (NA2). Those two examples, detailed above, are among the best exposed examples in this study and display a clear lithologic distinction between olivine-bearing and pyroxene-bearing units, with olivine ranging from fayalitic compositions in Alga to intermediate compositions in Ostrov. The pyroxenes for both regions were consistent with a high-Fe, low-Ca composition.

[36] An additional example from this region, NA4, is a 22 km diameter unnamed crater in the Northeast part of Ladon Basin (16.71°S, 28.14°W, Figure 16) that is contained within CRISM observation FRT000097FF. This example highlights the difficulty in determining the original context of excavated peak material. The crater impacts into the Ladon Basin that was strongly modified and filled. The Ladon Basin itself sits on crust strongly modified by previous impact and volcanic processes. This makes it difficult to determine the original context and origin of the crustal materials exposed in the crater's central peak. The central pit of NA4 is filled with aeolian materials, but the pit rim, particularly the northeastern portion, is comprised of mafic-bearing blocks. Light-toned olivine-bearing units form much of the northern and eastern pit rim, while pyroxene units dominate the western and southwest sides of the central pit. Two olivine-bearing regions were successfully modeled with compositions of Fo_{20} and Fo_{16} (Table 3). These values are among the most fayalitic in this region but are comparable to the range from Alga Crater (NA1). Three pyroxene regions were modeled with 2 μm NBSR values consistent at 0.56 (Table 4) with absorption bandcenters just above the LCP end-member values supporting the LCP enrichment of the pyroxene-bearing units.

[37] *North Hellas*. The North Hellas (NH) region contains nine well-defined and exposed central peaks covering a wide spatial distribution. Here we describe one example, NH6, a relatively small (20 km) crater on the northern edge of Hellas Basin (31.43°S, 81.63°W, Figure 17). The upper layers of the central peak, just below peak's apex are distinguished by a light-toned olivine-bearing lithology that is preferentially eroded from the darker surrounding material. The apex of the peak retains this darker material with a distinct pyroxene signature. One olivine region was successfully modeled yielding a three band fit with a composition of Fo_8 (Table 3). This observation is the most Fe-rich olivine-bearing site from the NH region, which are all consistently fayalitic within the fifteen olivine-bearing NH regions and show a full range from Fo_8 to Fo_{38} (Table 5). One pyroxene-bearing region from NH6 was modeled with an intermediate 1 μm NBSR (0.48) and LCP-rich 2 μm NBSR (0.73) (Table 4). While some variation does exist the pyroxenes from the Northern Hellas region consistently show a moderate to high LCP enrichment.

[38] *Nili Fossae*. The third region examined is the smallest current sample set with only two sites due to the high degree of alteration in this area [*Ehlmann et al.*, 2009]. The Nili Fossae (NF) region is classified as Southern Highland terrain but is

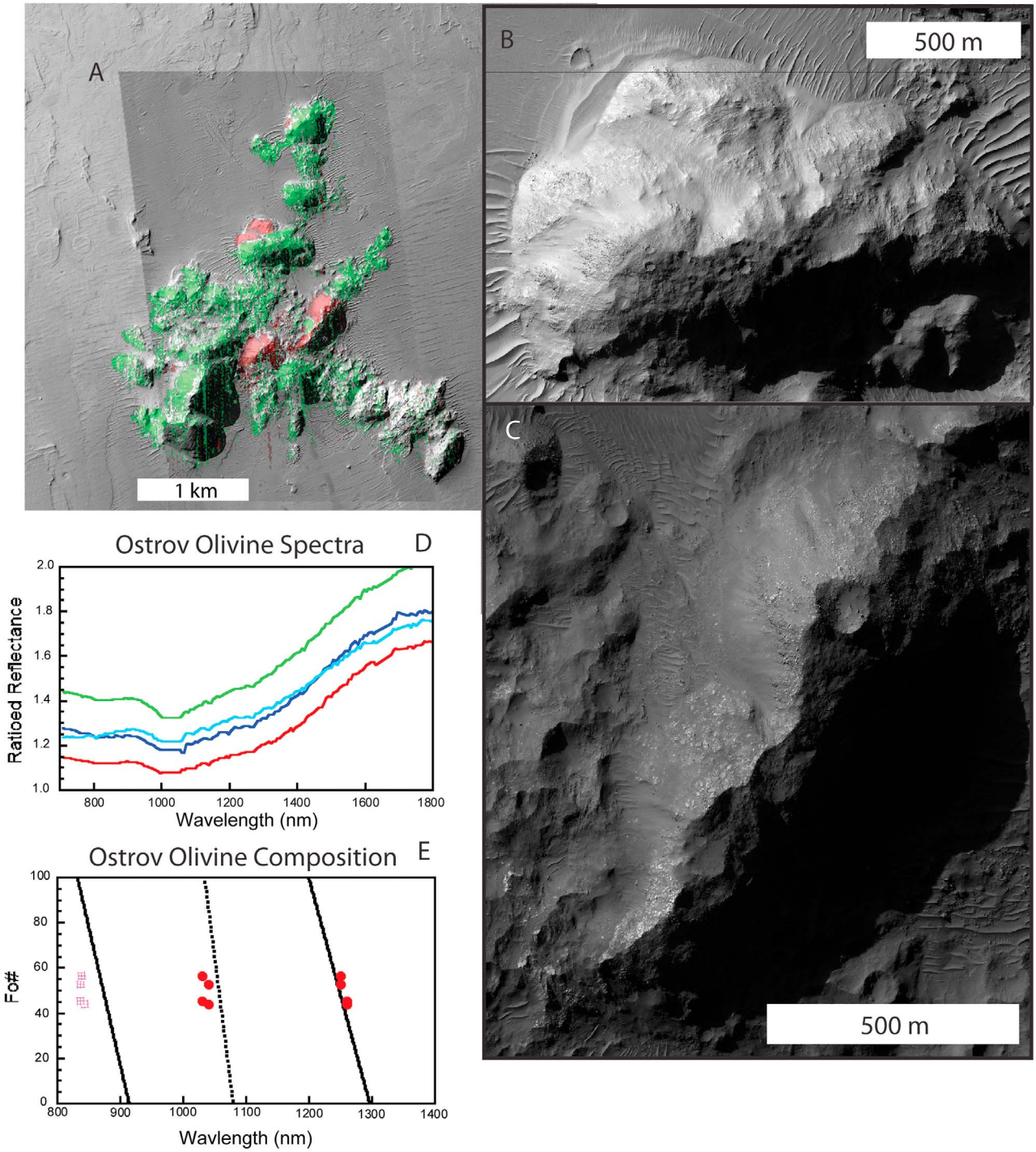

Figure 13. Ostrov crater. (a) Ostrov crater with CRISM parameter overlain on HiRISE and CTX. (R:Ol2index, G:LCPindex, B:HCPindex). CRISM:FRT00017D02, HiRISE: PSP_017357_1530, CTX: P17_007639_1514_XN_28S027W. (b) HiRISE of northern olivine deposit. (c) HiRISE of eastern olivine ridge. Shows olivine-bearing light-toned clasts. (d) Ratioed olivine spectra used in analysis. (e) Degraded S detector data (700 nm–1000 nm) caused bad band fitting results. Composition is determined with M2 and M1–2 expressed in L detector (1000 nm–1800 nm). Results in Table 3.

located on the western edge of the Isidis basin and just south of the dichotomy border. The Nili Fossae region has been well examined due to well-exposed bedrock and a diverse geologic history [e.g., *Hoefen et al.*, 2003; *Mangold et al.*, 2008; *Fassett and Head*, 2005; *Mustard et al.*, 2009; *Ehlmann et al.*, 2009]. Both craters are similar in size and each contains exposures of olivine and pyroxenes. Here we detail Hargraves (NF1) (20.76°N, 75.81°E, Figure 18) with a central pit structure that is dominated by pyroxene-bearing bedrock with a few small olivine outcrops around the pit.

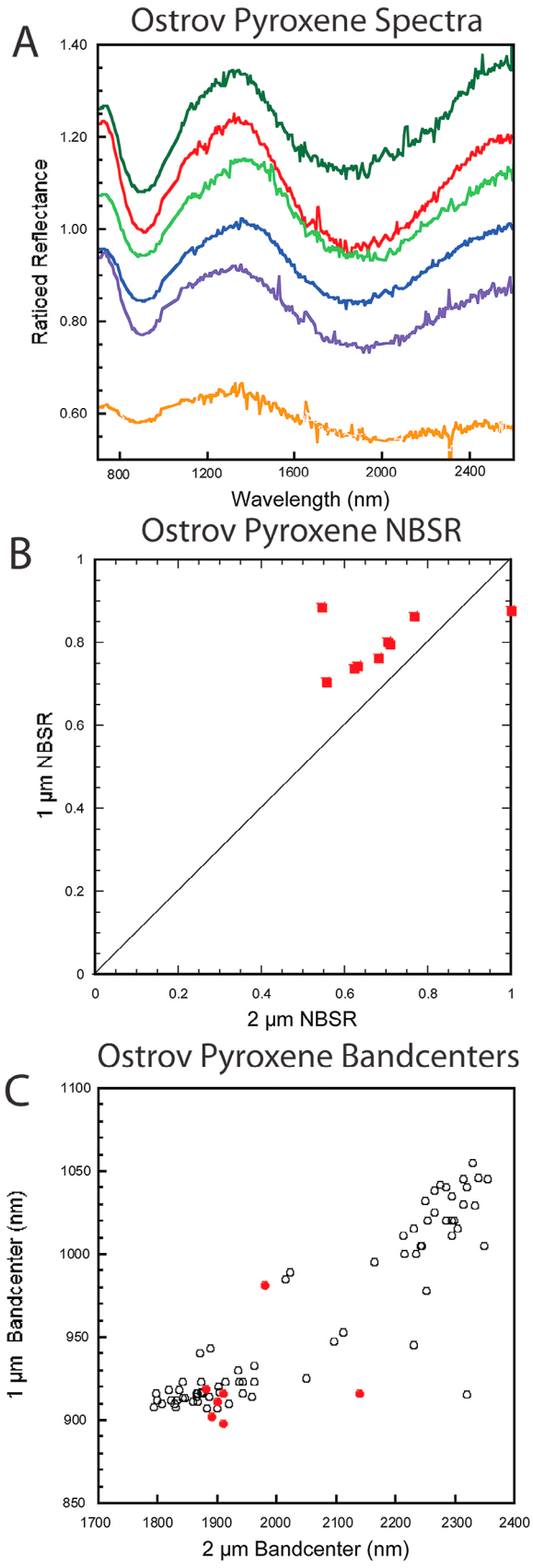

Unlike most of the other examples, the olivine-bearing material does not correlate to a clear difference in tonality. The modeled olivine region in this central peak had a composition of Fo_{14}, while the range for the six modeled regions in NF have a range of $Fo_{5–14}$, again showing a strong fayalite enrichment. Pyroxene modeling of six regions in NF1 results in range of a 2 μm NBSR of 0.56–0.63 with a similar range for the 1 μm, again consistent with a slight enrichment in LCP.

[39] *Northern Plains*. The North Plains (NP) region includes six craters with concentrations in Acidalia Planitia (NP1, NP2) and Utoipia Planitia (NP3-NP6). Two sites, Kunowsky Crater (NP1) and Stokes Crater (NP5), are relatively large at 60 km, while the other four are 30 km or less, all of which are large enough to penetrate the Hesperian basalts that resurfaced the lowlands and that are estimated to be hundreds of meters thick [*Head et al.*, 2002]. The four smaller craters all contain well-formed and preserved central peak structures surrounded in part by dark, olivine bearing dune materials. These are identified by the low albedo compared to the noticeably brighter olivine bedrock. In selecting regions of interest we choose spatially continuous mafic units based on the spectral parameter maps. With this method, central peaks in the Southern Highlands contained at most nine modeled olivine regions and in some cases only one or two regions. In contrast, the large NP craters, Kunowsky (NP1) and Stokes (NP5) have 17 and 21 olivine-bearing outcrops respectively.

[40] Stokes Crater (NP5) (Figure 19) contains one of the more complex central peak structures examined in this study. The peak itself is offset to the north of center of the crater with depressions to the south and east of center. Large diffuse light-toned olivine-bearing units outcrop from the peak and edge of the southern basin. In between the olivine exposures on the peak are small pyroxene-bearing units. The eastern depression contains dark olivine-bearing dunes which overlie light-toned, highly fractured megaclasts with strong olivine signatures. The 21 modeled olivine regions yield a diverse compositional range of $Fo_{15–65}$ ranging from mildly forsteritic to strongly fayalitic. The 2 μm pyroxene NBSR values for the 16 modeled regions range from 0.53 to 0.62 with values for the 1 μm absorption about 0.1 less (Table 4). Stokes Crater fits into the pattern we are observing across the planet with light-toned olivine breccia interspersed with pyroxene bedrock units.

[41] These regional examples show strong similarities among the observed central peak mafic units. In all the locations we observed megaclasts with no evidence of spectral mixing. The observed olivine range from moderately forsteritic to strongly fayalitic and the pyroxene units are consistently enriched in LCP. Here we present the composition results of all the regions to determine any regional or global trends.

[42] *Nature of Olivine Compositional Trends*. MGM modeling of the olivine regions from all of the sites show a wide range of values from Fo_5 to Fo_{70} (Figure 20a and Table 5) with

Figure 14. Ostrov Pyroxene. (a) Ratioed Ostrov pyroxene spectra. (b) Ostrov Pyroxene NBSR results consistent with LCP-enrichment. (c) Ostrov pyroxene 1-, 2 μm band centers plotted against terrestrial pyroxene band centers [*Adams*, 1974; *Cloutis and Gaffey*, 1991]. From bottom left to upper right, pyroxene composition goes from Mg-rich to Fe-rich to Ca-rich. Ostrov pyroxene plot as low-Ca, moderate Fe with some outliers. Results in Table 3.

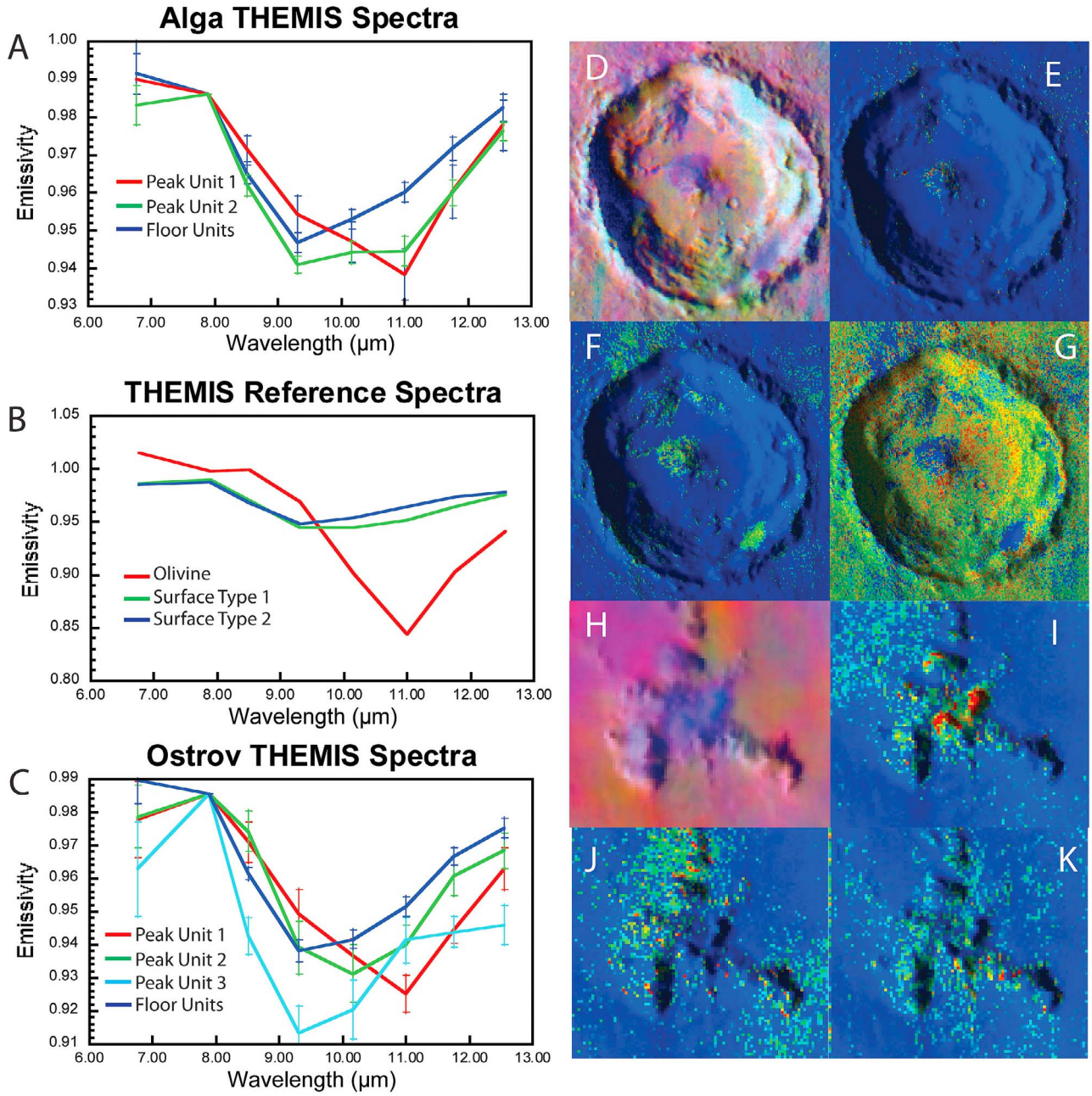

Figure 15. THEMIS thermal results. (a) Alga THEMIS spectra from end-member regions. (b) Reference end-member library spectra. Laboratory measured olivine spectra, Mars derived Surface Type 1 and 2 [*Bandfield et al.*, 2000]. (c) Ostrov THEMIS spectra from end-member regions. (d) Alga DCS (9,6,4) highlighting the mafic mineralogy. (e) Alga Peak Unit 1 end-member map. The end-member has the distinct feature at 11 μm consistent with the olivine lab spectra. (f) Alga Peak Unit 2 end-member map. (g) Alga Floor Units end-member map. (h) Ostrov DCS (9, 6, 4) highlighting the mafic mineralogy. (i) Ostrov Peak Unit 1 end-member map. (j) Ostrov Peak Unit 2 end-member map. K) Ostrov Peak Unit 3 end-member map.

a mean value of Fo_{28} for all regions. This reinforces the Fe-rich fayalitic nature of the observed olivine units but highlights the diversity in the compositions. NA olivine-bearing units have a mean of $Fo_{34\pm23}$ (Figure 20b). This region has the highest Fo of the four regions as well as the largest range. NH has a mean of $Fo_{18\pm7}$. The NH sites (Figure 20c) are systematically fayalitic with only a small variation indicating a clear difference from the composition distribution in NA. NF has only 6 modeled regions and contains the most fayalitic values with a mean of Fo_{10} and a narrow 4 Fo unit range. The NP region (Figure 20d) has a composition distribution similar to NA with a mean of $Fo_{32\pm15}$, and can be subdivided into the Acidalia and Utopia populations. The Acidalia region (NP1, NP2) has a range of Fo_{11-58} with a mean of Fo_{43}, while Utopia (NP3, NP4, NP5, NP6) has a range of Fo_{7-56} with a mean of Fo_{26}. The olivine in the Acidalia region is significantly more Mg-rich than Utopia

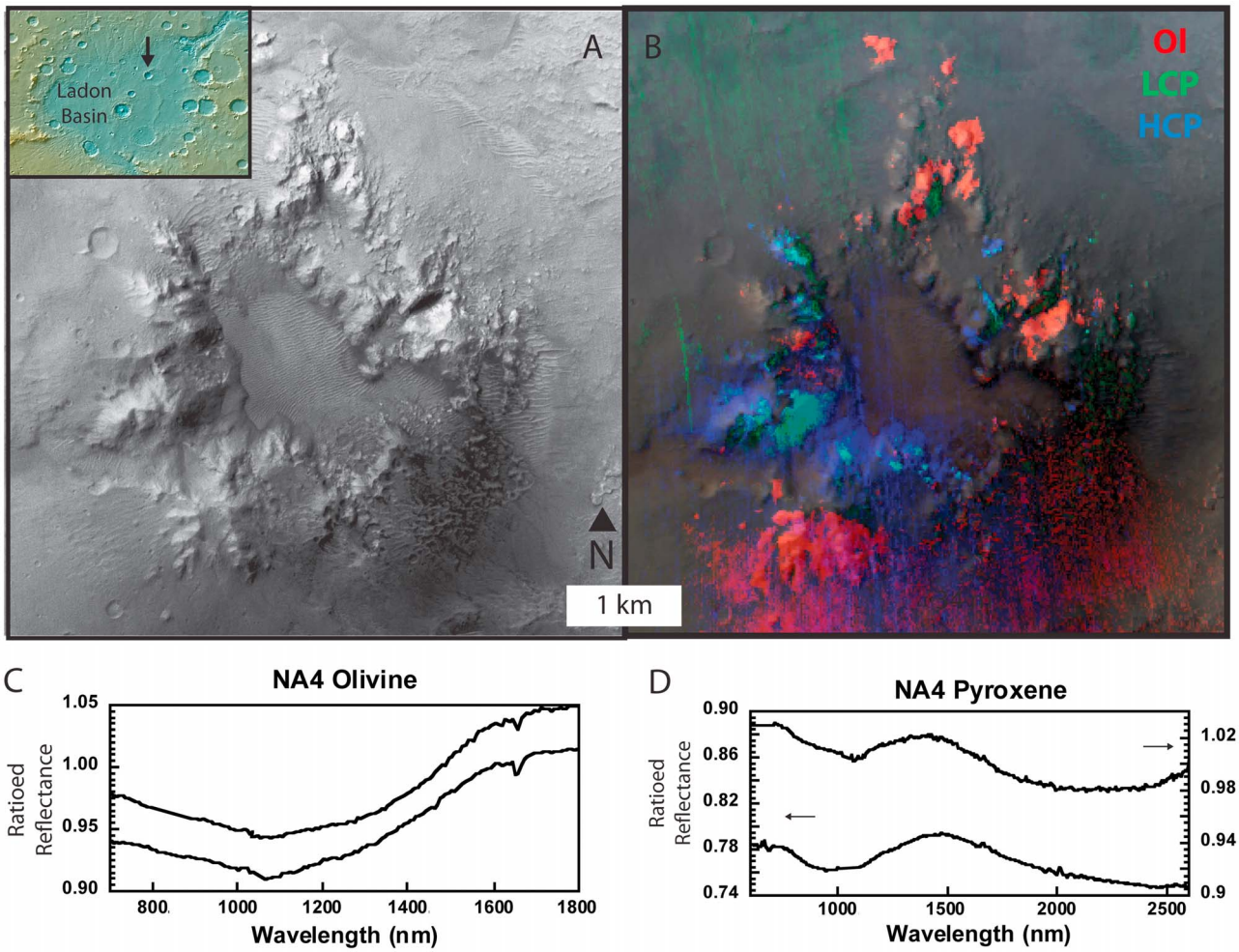

Figure 16. North Argyre example region. Ladon Basin context (Figure 1a, inset) with arrow pointing to crater that contains this central pit structure. (a) NA4 is one of the few sites that have a central pit. (CTX). (b) Mineral map showing mafic deposits on central pit structure. (CRISM FRT00097FF Parameter Map R: Olindex2 G:LCPindex B:HCPindex on CTX). (c) Ratioed Olivine Spectra. (d) Ratioed Pyroxene Spectra.

highlighting the regional differences that are emerging from the observations (Table 4).

[43] *Pyroxene Bandcenter Analysis*. Modeling the pyroxene absorptions with 2 absorptions to get bandcenter allow the comparison of regional compositions to terrestrial pyroxene values. Figure 21 plots the modeled bandcenters against a set of laboratory measured CPX and OPX [*Adams*, 1974; *Cloutis and Gaffey*, 1991]. The 2 μm bandcenters for the NF (Mean:1897 nm) and NA (Mean:1922 nm) regions are lowest and consistent with low-Ca, moderate-Mg pyroxene end-member (pigeonite). The NH area pyroxenes have higher 2 μm bandcenters (Mean:1962 nm) indicating higher Fe content but still low-Ca (ferrosilite). The 2 μm bandcenters for the NP (Mean:1965 nm) have a wide spread but are generally elevated compared to the Southern Highland pyroxenes with many comparable to moderate Ca compositions (pigeonite).

[44] *Pyroxene NBSR Analysis.* MGM modeling of the pyroxene unit spectra with five absorptions allow for the determination of the relative proportions of low and high-calcium pyroxene components by calculating the NBSR value for both the 1 and 2 μm absorptions (Figure 22 and Table 6). This provides an additional composition consistency check as a well measured and modeled pyroxene should have consistent NBSR values for both absorptions. Here we observe an agreement between the 1 and 2 μm was within 0.04 for the Southern Highland sites and 0.08 for the Northern Lowland sites (Table 6). Comparing between regions highlights additional regional differences in composition. The three Southern Highland regions show a consistent LCP enrichment with a slight difference between regions while the NP sites have a noticeable HCP enrichment.

[45] A final analysis was performed to look for compositional trends as a function of central peak excavation depth. No detectable trends were determined as either a function of excavation or crustal thickness. The degree of vertical mobility of the central peak materials from the past cratering processes seems to have swamped any remnant compositional stratigraphy that may have existed.

[46] *TES Thermal Infrared Constraints*. A dedicated analysis of Martian central peaks with the TES thermal IR instrument is currently underway [*Pan and Rogers*, 2011]. While many of the craters and all of the spectral units detailed in this study are too small for TES analysis, two sites (NA3 and NH3) have been analyzed by *Pan and Rogers* [2011].

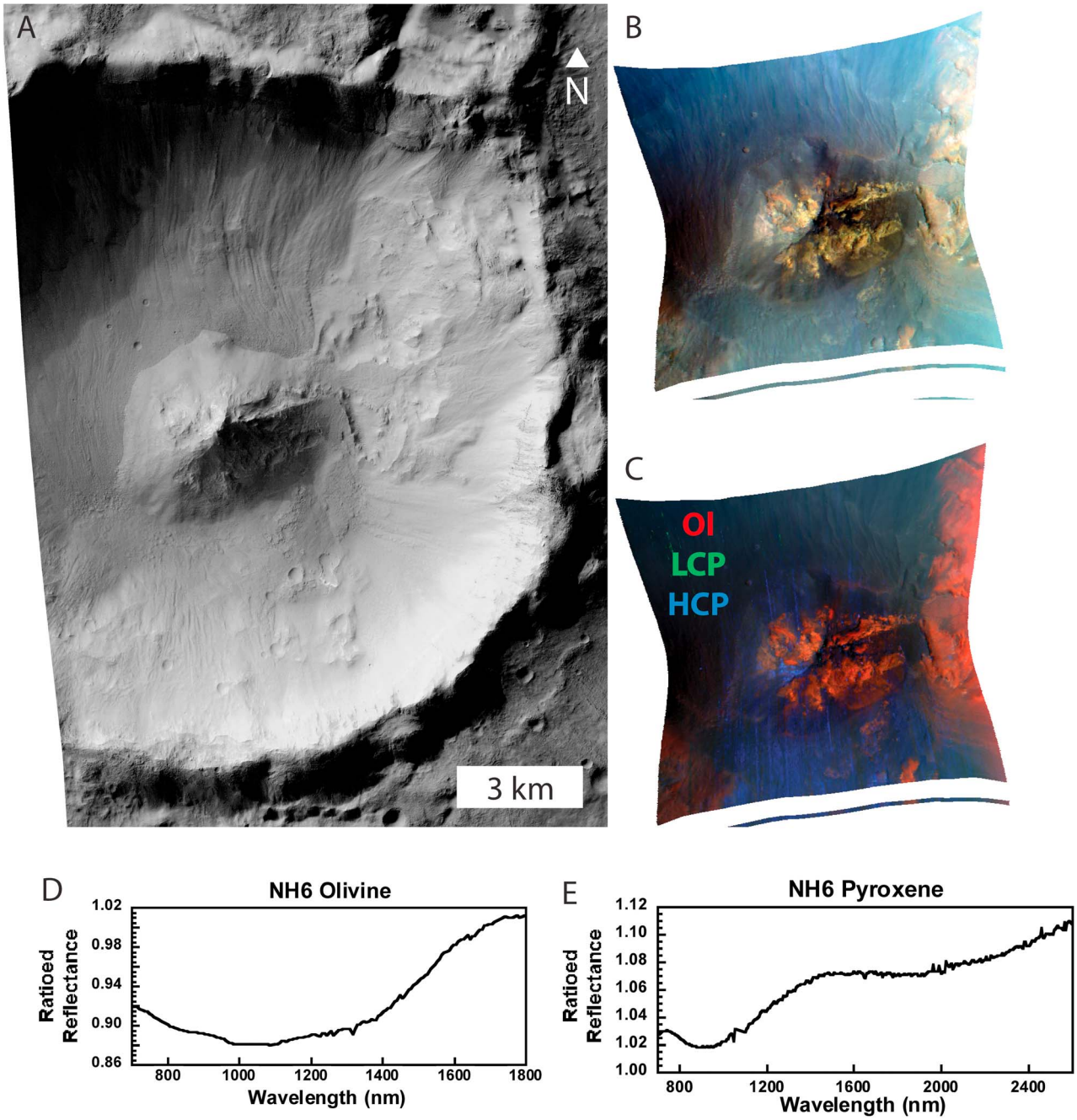

Figure 17. North Hellas example region. (a) NH6 is a classic central peak structure with a ring of light-toned olivine and a peak of pyroxene-bearing material. (b) CRISM Projected RGB. Observation is 10 km across at center. R:2.5 μm G:1.5 μm B:1 μm (FRT0001EBA0). (c) CRISM projected mineral map showing mafic deposits on central pit structure. CRISM Parameter Map R:Olindex2 G:LCPindex B:HCPindex. From CRISM: FRT0001EBA0. (d) Ratioed Olivine Spectra. (e) Ratioed Pyroxene Spectra. From CRISM: FRT0001EBA0.

While the results are still preliminary, these two sites were grouped with several others with a similar thermal spectral response and classified as relatively feldspar rich with a collective compositional abundance of 32% Feldspar, 19% LCP, 17% HCP, 0.1% Olivine and 14% High-silica phases with the remaining 18% as accessory phases and blackbody. The spatial resolution differences between instruments and the several central peak averages in this study make a direct comparison difficult but point out the significant feldspar component that is not characterized by CRISM observations and has potential for future development.

5. Discussion

[47] Considering the single plate nature of Mars, crater central peaks are the best source of exposed buried crustal

Table 5. Summary of Modeled Olivine Composition Results[a]

	Regions	Fo Range	Fo Mean	Fo SD
NA Olivine	18	7–70	34	23
NH Olivine	15	8–38	18	7
NF Olivine	6	5–14	10	4
NP Olivine	87	7–58	32	15

[a]Region; Number of modeled spectra in the region; Range of modeled values; Mean modeled composition of all regions; Standard deviation of modeled compositions. Table summarizes full results in Table 3.

material, the history and context of that material is dependent on the complex history of the local area. The basement rocks of Alga crater could include ejecta from Argyre basin to the south and is within the outer rings of Ladon basin and Chekalin crater. This history would have resulted in intense brecciation of the crust, redistribution and burial of impact products (e.g., melts), and potentially basin related volcanism [*Schultz and Glicken*, 1979]. This local complexity makes constraining the ancient crust from these exposures a difficult task.

[48] *Implications of Global Distribution*. The selection of these 23 central peak structures was the result of considering CRISM observed unaltered, mafic bearing central peaks. After identification and successful modeling of the mafic spectra extracted from the central peaks, the locations were plotted and the four regional groupings were identified (Figure 2). These resulting groupings are possibly the result of several properties of the Martian surface or may provide deeper understanding of the nature of these exposed units. A

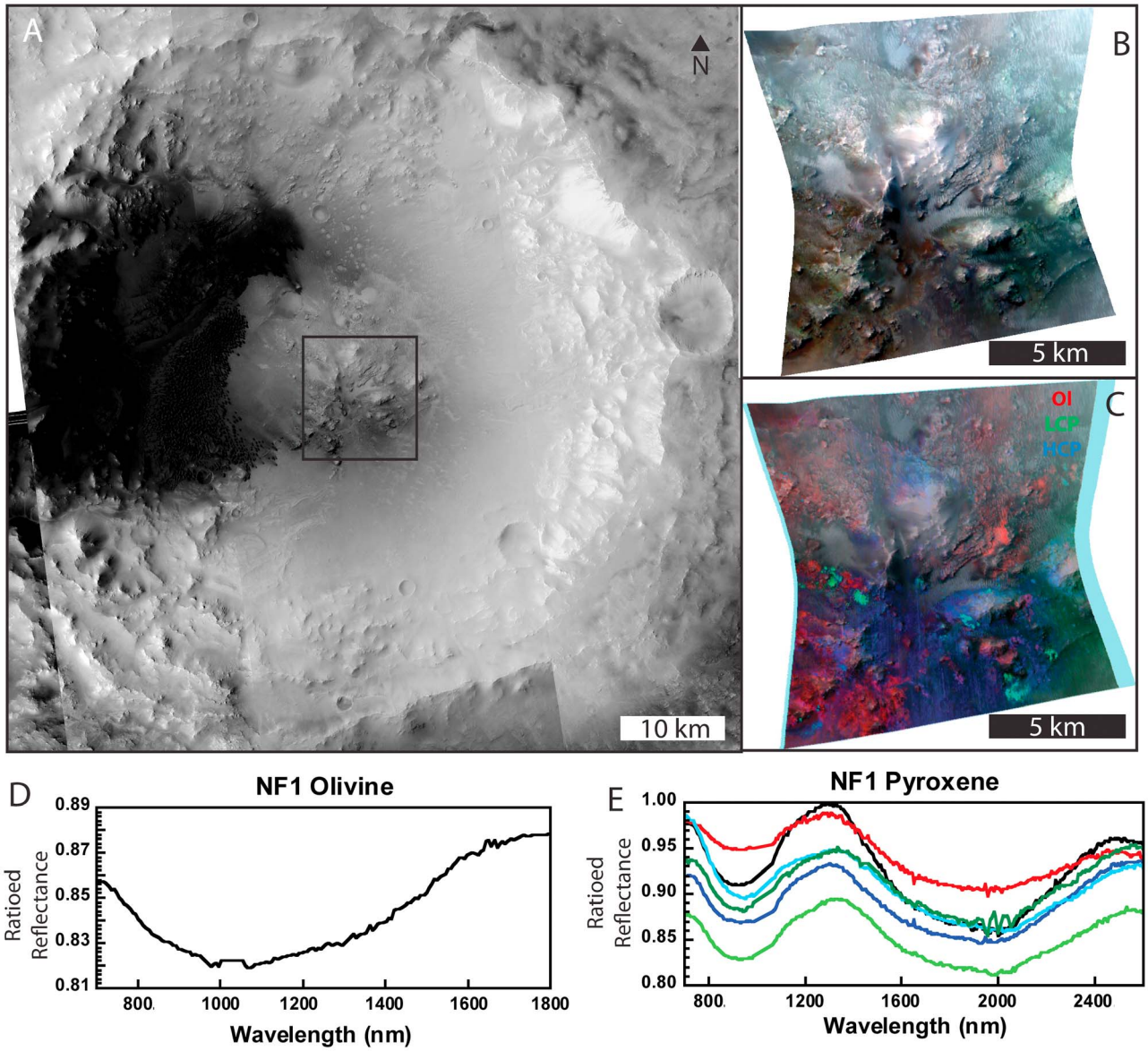

Figure 18. Nili Fossae example region. (a) NF1 CTX overview of Hargraves crater. (b) CRISM projected mineral map showing mafic deposits on central pit structure. Observation is 10 km across at center. R:Olindex2 G:LCPindex B:HCPindex. (c) CRISM Projected RGB. R:2.5 μm G:1.5 μm B:1 μm (FRT0000B573). (d) Ratioed Olivine Spectra. (e) Ratioed Pyroxene Spectra. From CRISM: FRT0000B573.

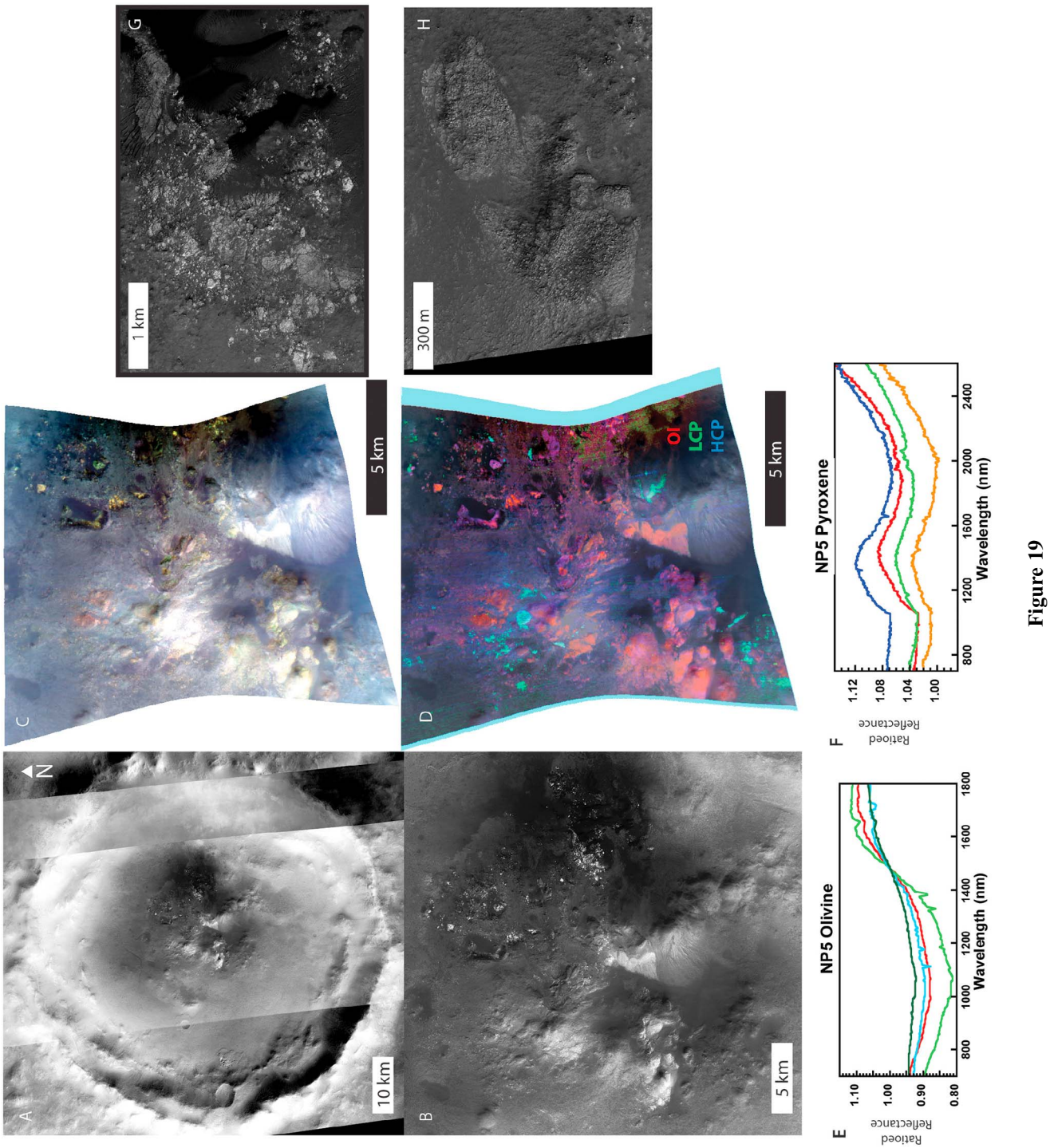
A
N
10 km
B
5 km
C
5 km
D
Ol
LCP
HCP
5 km
G
1 km
H
300 m
E
Ratioed Reflectance
NP5 Olivine
1.10
1.00
0.90
0.80
800
1000
1200
1400
1600
1800
Wavelength (nm)
F
Ratioed Reflectance
NP5 Pyroxene
1.12
1.08
1.04
1.00
800
1200
1600
2000
2400
Wavelength (nm)

Figure 19

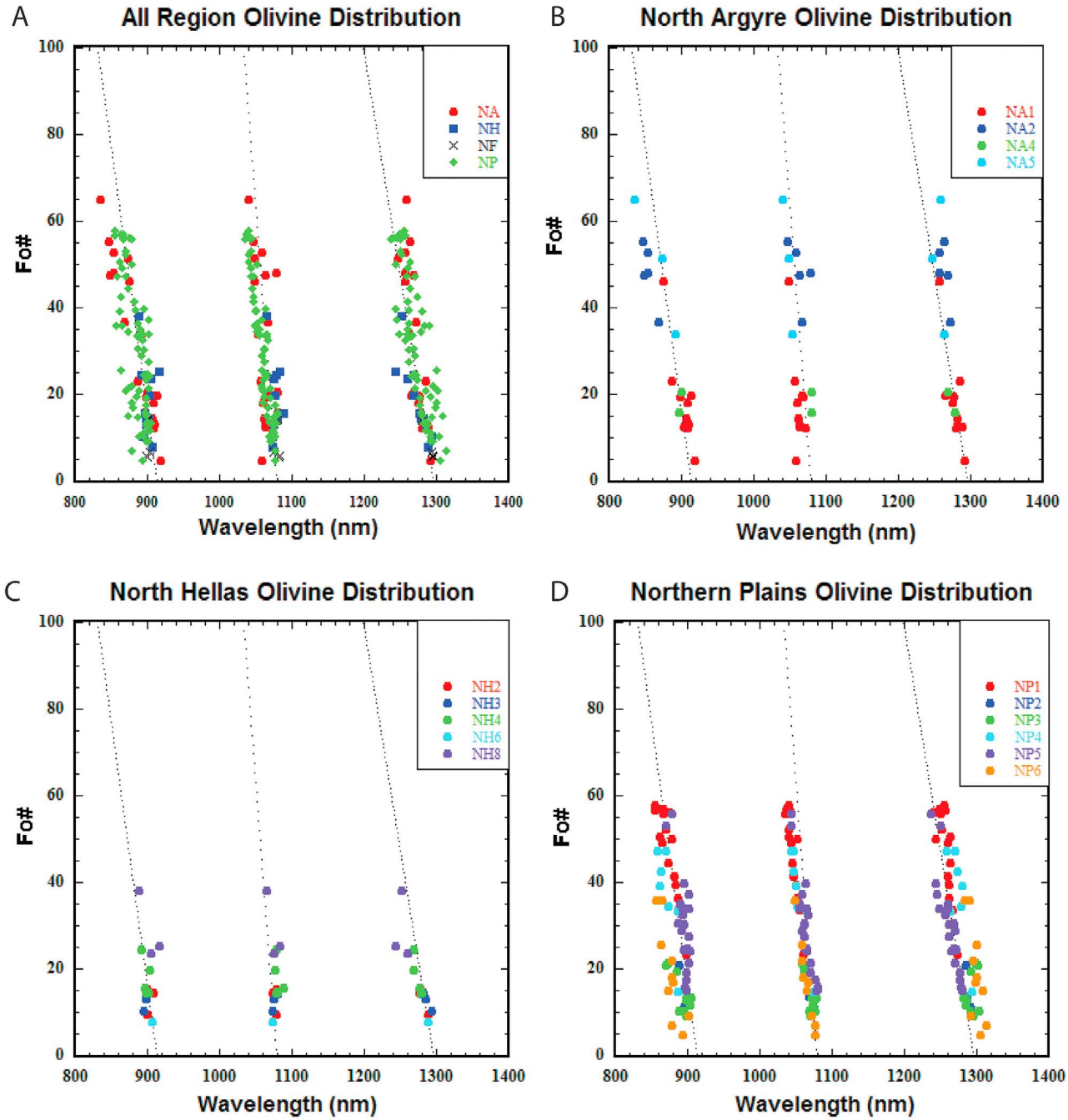

Figure 20. (a) All Outcrop Olivine Distribution. Plot shows the modeled composition for all examined olivine regions. (b) Argyre Olivine Outcrop Distribution. (c) Hellas Olivine Outcrop Distribution. (d) Northern Plains Olivine Outcrop Distribution. All plotted data is in Table 3.

Figure 19. Northern Plains example region. (a) NP5 Context image of Stokes Crater (CTX). (b) CTX view of central peak. Light-toned small clasts in upper right are classic olivine-bearing breccias. Lower right light material are olivine bearing particulate material not used for olivine analysis. (c) CRISM projected mineral map showing mafic deposits on central pit structure. Observation is 10 km across at center. R:Olindex2 G:LCPindex B:HCPindex (CRISM FRT0000ADA4). (d) CRISM projected RGB. R:2.5 μm G:1.5 μm B:1 μm (CRISM FRT0000ADA4). (e) Ratioed Olivine Spectra. Poor registration from the S detector are unable to resolve the 1 μm pyroxene absorption, causing increased error with three band olivine fitting. This is a case when the two band fits would provide more confident results. (f) Ratioed Pyroxene Spectra. From CRISM: FRT0000ADA4. NP5. (g) Light-toned olivine-bearing breccias exposed in the depression just east of the Stokes Crater center. (h) Pyroxene-bearing bedrock material exposed north of the Stokes Crater center. HiRISE: ESP_016980_2360.

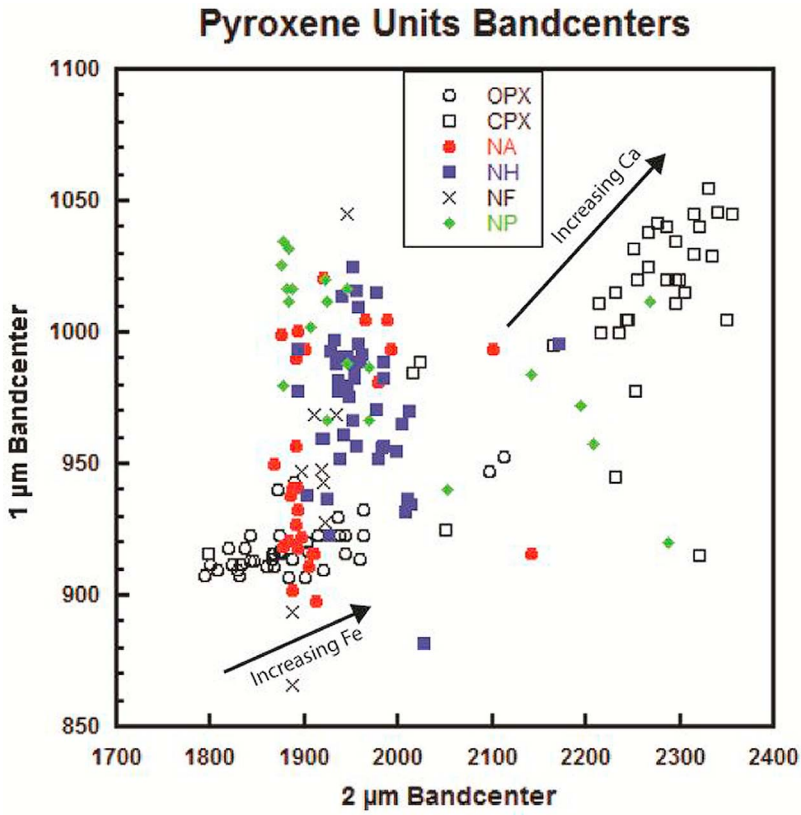

Figure 21. Pyroxene Bandcenters: 1-, 2 μm bandcenters of all pyroxene regions plotted against terrestrial pyroxene bandcenters [*Adams*, 1974; *Cloutis and Gaffey*, 1991] by region. From bottom left to upper right, pyroxene composition goes from Mg-rich to Fe-rich to Ca-rich. Plot of modeled pyroxene bandcenters plotted against terrestrial laboratory measured bandcenters. Significant variation exists on the 1 μm axis while the 2 μm axis is well modeled. While variation exists in each region, averages vary from low-Fe, low-Ca toward high-Fe, high-Ca in the order of North Argyre, North Hellas, Nili Fossae, and Northern Plains. Variation in 1 μm modeled could be a contribution of olivine in the spectrum or L-S detector alignment problems. The addition of glass could also shift the bandcenters to longer wavelengths. All plotted data is in Table 4.

similar distribution is observed in the overall distribution of the Crater Exposed Bedrock Database [*Tornabene et al.*, 2010] that considers only the HiRISE morphology and not the mafic spectroscopy, indicating that is it more than just an effect of surface spectral quality. Several surface properties that may contribute to the observed distribution, including dust cover [*Ruff and Christensen*, 2002], crater density, bedrock exposures and outcrop surface refreshing rates, and the presence and pervasiveness of alteration. For example, the volcanically dominated areas of Tharsis and Elysium lack observations in this study due to the lack of preserved craters and the high dust cover [*Ruff and Christensen*, 2002] of these elevated regions. While conclusive evidence for this regional discrepancy is elusive, we offer several possible explanations assuming that the observation is real and not solely an artifact of the current CRISM FRT coverage. One hypothesis is that the concentration around the main Martian basins (Argyre, Hellas, Isidis, and Utopia) is not coincidental and that the reported central peaks are excavating ejecta materials that were created and/or redistributed by these basins. The effect of the basin excavation could potentially allow a source from the lower crust or even the Martian mantle. Another possibility is that the regions outside of our listed sites are regions of heavy crustal alteration, so that minimally altered central peaks are no longer observed there. This option is unlikely due to the correlation of the observations in the Crater Exposed Bedrock Database [*Tornabene et al.*, 2010], which are based on morphology and not composition. A third possibility is that the regions without reported observations have lower abundance of well-exposed crustal bedrock. For instance, the lack of exposed mafics at southern midlatitudes (30°S–60°S) may be due to mantling deposits covering the bedrock [*Mustard et al.*, 2001]. This would explain the lack of observations to the south of Argyre and Hellas Basin and toward the polar regions. One final hypothesis is that the bedrock exposures we are describing are not globally distributed. It could be that the textures and morphologies we are documenting are plutonic in origin and that we are observing the excavated remnants of large but localized volcanic plumes occurring below places like the North Argyre and North Hellas areas where the crust has been compromised by the formation of these large basins. Future mapping and additional understanding of the observed lithologies may help decide between these hypotheses.

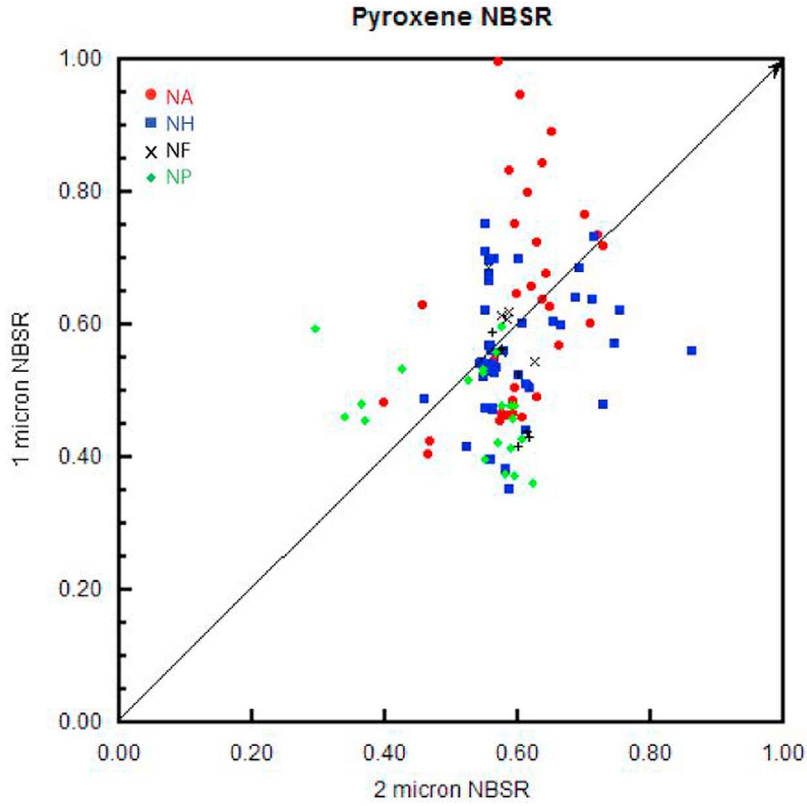

Figure 22. Pyroxene NBSR. LCP/(LCP+HCP) Band depths. NBSR for all modeled pyroxene observations, colored by region. Significant variance exists on the 1 μm axis while 2 μm NBSR shows regional differences. In order of decreasing LCP, the regions rank North Argyre, North Hellas, Nili Fossae and Northern Plains. Data summarized Table 2 and detailed in Table 4.

[49] *Lithology Determination*. VNIR spectroscopy of mafic minerals is sensitive to cation composition of the dominant mineralogy but may not detect minerals without a distinct near-infrared signature or sufficient abundance. Rock compositional results must then include assumptions about the target materials and an understanding of the VNIR and TIR spectroscopic ranges. One notable limitation with the VNIR spectral range is that the plagioclase absorption feature can only be observed if it contains trace amounts of Fe^{2+} and is present in extremely high abundances (>~85%) [*Bell and Mao*, 1973; *Nash and Conel*, 1974; *Crown and Pieters*, 1985; *Cheek et al.*, 2011]. The strong mafic signatures of the units reported here overwhelm any potential signature from plagioclase, limiting our ability to reliably report on its presence, abundance and composition with the VNIR observations. The application of THEMIS IR observations are able to help constrain the silicate compositions though they have spatial and spectral resolution limits. Near-infrared observations are well suited for the detection of Fe-bearing olivine and pyroxene minerals. The compositional determination of the Alga olivine-bearing lithology focuses on the complete absence of a 2 μm pyroxene absorption indicating pyroxene content less than ~5–10% and THEMIS observations show spectra consistent with an olivine end-member. These observations indicate that this unit has a mafic only composition in the range of a dunite (>90% olivine) composition with a fayalite composition ranging from Fo_{45-7}. The coupled THEMIS observations however indicate some degree of feldspar mixing, suggesting a trOctolite-dunite composition.

[50] The pyroxene-bearing lithologies are interpreted using similar reasoning. The 1 μm region can be fully modeled with the expected pyroxene absorptions without requiring an olivine component at slightly longer wavelengths. VNIR observations indicate nearly pure pyroxene with olivine content less than 5%, suggesting a pyroxenite lithology (although spectral analysis cannot rule out a borderline noritic composition). This is consistent with but not uniquely confirmed by the THEMIS observations. The band centers of the observed pyroxenes are both in the low range on the pyroxene continuum indicating low-Ca content but the relativity long-wavelength band center of the 1 μm absorption, while still in the LCP range, suggests a Fe-enrichment. While there is some spread to the observations

Table 6. Summary of Modeled Pyroxene Composition Results[a]

	Regions	1 μm NBSR Mean	1 μm NBSR SD	2 μm NBSR	2 μm NBSR SD
NA Pyroxene	32	0.65	0.14	0.62	0.09
NH Pyroxene	46	0.56	0.09	0.60	0.07
NF Pyroxene	12	0.55	0.08	0.59	0.02
NP Pyroxene	30	0.46	0.07	0.54	0.09

[a]Region; Number of modeled spectra in the region; Mean 1 μm NBSR values; Standard deviation of 1 μm NBSR values; Mean 2 μm NBSR values; Standard deviation of 2 μm NBSR values. Table summarizes full results in Table 4.

they are generally consistent with an enrichment of low-calcium and relatively high-Fe cation content. These results would signify an average composition in the range of a Fe-rich pigeonite. However, large scale spatial mixing would have difficulty discriminating between pure pigeonite and an intimate mixture of end-member minerals such as an augite-ferrosilite mixture.

[51] The light-toned pyroxene unit also shows no evidence of VNIR spectral mixture with other minerals and is similar in cation composition to the pyroxene-bearing bedrock with weaker band depth. We suggest that this is most easily explained as a mixture with the pyroxene-bearing bedrock and a VNIR spectrally featureless material, possibly the impact melt deposited on or injected into the exposed bedrock of central peak, or potentially, a plagioclase phase that would increase reflectance but not affect the VNIR observation. This would have the effect of attenuating the absorption feature band depth but keeping the band centers fixed as observed [*Tompkins and Pieters*, 2010]. Current thermal observations are too coarse to determine the pyroxene proportion of the unit or the bright phase.

[52] The impact melt unit is dominated by a bland spectral signature with a small proportion of pyroxene causing weak absorptions. The position of the fine grained impact melt unit in the overall unit stratigraphy is still uncertain, but we suggest two possible scenarios. The first is that the impact melt formed from the pyroxene bedrock unit during the formation of Alga crater and it covered a portion of the central peak, entraining clasts of pyroxene-bearing material. This scenario is supported by the presence of possible flow like features (seen in Figures 6 and 11) that could represent the remnants from the early flow of these hot materials, prior to solidification. However, Alga crater over time has been eroded and may be expected to wear away a surficial veneer of impact melt. The second scenario is that an impact melt component was produced in a previous basin scale impact event (e.g., Ladon or Argyre basin formation) and was emplaced as part of deep crustal stratigraphy and subsequently excavated by Alga. The relatively weak nature of the melt would cause preferential erosion and the observed recession of this unit.

[53] The central peak of Ostrov crater has only two discernible units and, unlike Alga, these are only easily distinguished with spectral mapping. The units are an olivine-bearing unit seen in three locations and a pyroxene-bearing unit comprising the rest of the central peak (Figure 13). Similar to the Alga units, we observe no mafic mixing in the VNIR or TIR, again indicating that the units are dominated by a single mafic phase and are interpreted to be dunite (or trOctolite) and orthopyroxenite (or norite) respectively. The olivine-bearing unit has significantly higher Fo# than the Alga olivine units. While it is difficult to draw conclusions about the exposed crust from two examples, we note compositional diversity and relatively high Fe contents compared to most of the reported values from other Martian olivine samples, typically ranging from $Fo_{30–80}$ [*Hoefen et al.*, 2003; *Koeppen and Hamilton*, 2008; *McSween et al.*, 2006; *Edwards et al.*, 2008; *Tornabene et al.*, 2008]. The Ostrov pyroxene-bearing unit is compositionally similar to the Alga pyroxene unit characterized by high-Fe, low-Ca pyroxene.

[54] These two crater central peaks offer a look into the composition of the deep crust of Mars. While not representative of the whole crust, we begin to see some important trends. The first is that in both examples we observe cumulate outcrops, dunites and pyroxenites, with no evidence of mixtures of these minerals. This may indicate that the ancient crust was largely formed in large, slow cooling magma bodies similar to terrestrial large mafic intrusions [*Cawthorn*, 1996] rather than a series of quick cooling lava flows. The second is that the olivine displays a range of compositions from intermediate to fayalitic, with a significant Fe-enrichment compared to other measured Martian olivine. Finally, the observed pyroxenes seem to be dominated by a high-Fe, low-Ca calcium composition. This is consistent with the high Fe values seen in the olivine-bearing units and with the LCP pyroxenes seen in Noachian terrains throughout Mars [*Mustard et al.*, 2007].

[55] The observations that the ancient Martian crustal material has been mineralogically segregated with a range of Fe-rich compositions indicate that it had a crystallization history fundamentally different than the basalts that cover most of the surface [*Rogers and Christensen*, 2007; *Poulet et al.*, 2009]. This ancient crust would have had to experience crystal segregation into the observed dunites and orthopyroxenites. We note the similarity between these hypothesized cumulates and the units described by *Francis* [2011] for the Columbia Hills in Gusev Crater. These layers would have to be thick enough to become brecciated clasts several hundreds to thousands of meters across and must occur close enough in proximity that a single central peak can excavate both units. Only a few known methods exist for segregating minerals on large scales and we examine the possibilities.

[56] *Crustal Formation*. The complex cratering history of Mars makes it difficult to reconstruct the original stratigraphy of the exposed units, however only a few mechanisms are known to segregate mafic lithologies at kilometer scales. These include dunite channels in harzburgite as seen in ophiolites [*Kelemen et al.*, 1995] and olivine deposition from komatiite surface flows [*Walter*, 1998] or melt fractionation of basin induced impact melts [*Warren et al.*, 1996]. The first example has only been observed as a product of terrestrial plate tectonics in mid-ocean ridges, a feature not observed or expected on Mars. The second example would be unlikely to produce mineralogically segregated units thousands of meters thick as required by the spatial area of the observed blocks. The third option is viable and would potentially be difficult to distinguish from an internally erupted lava lake. The most commonly observed method for mineral segregation on Earth is a cumulate settling processes forming a layered mafic sequence. These features, well studied in variety of terrestrial locations from the Bushveld complex in South Africa to the Skaergaard intrusion in Greenland [*Cawthorn*, 1996] can produce the observed Martian lithologies at the observed scales. One well studied example is the Bushveld Complex in South Africa [*Cawthorn*, 1996]. The Bushveld complex has been divided into four zone from top to bottom, Upper, Main, Critical and Lower. We will specifically focus on the Upper Zone, the one that would be the most likely to be excavated by impacts. This unit contains olivine that range from $Fo_{63–5}$, a similar range observed in the Mars observations presented here. Orthopyroxenes in the Upper Zone range from a mg# 60–Mg#30 with most areas having values in the mid 50s mg#. The entire Bushveld complex is depleted in clinopyroxenes, again similar to our presented Mars observations. However, the Bushveld is only illustrative of the process that could have occurred on Mars. The Bushveld is the product of multiple

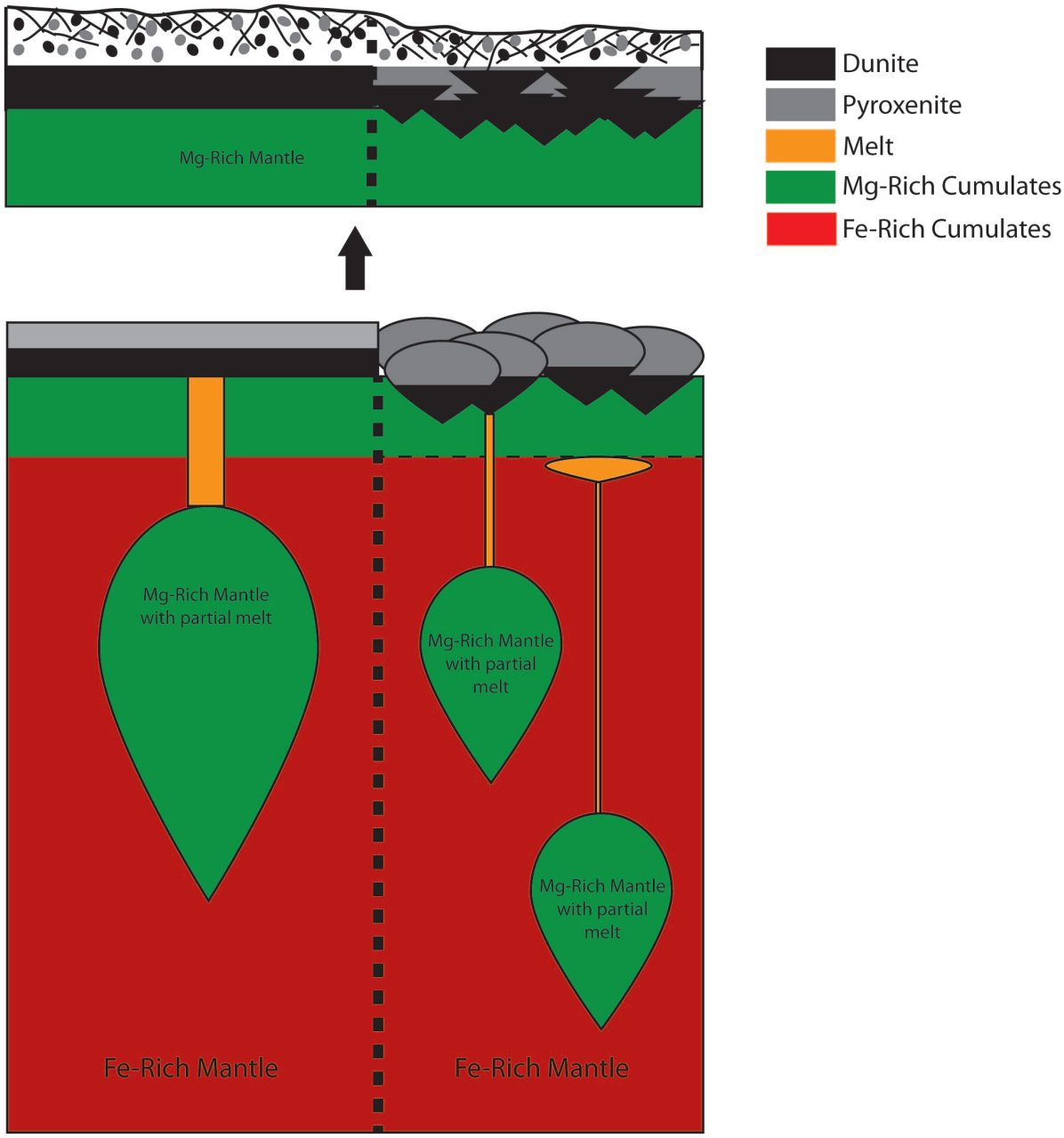

Figure 23. Proposed model of crustal formation. (bottom) Mantle density instabilities would lead to overturn with rising diapirs of Mg-rich minerals. Decompression melting would preferentially melt the Fe-rich faction which would buoyantly rise faster than the diapir. Large volume eruptions would cool slowly and stratify into cumulate layers. Figure 23 (bottom left) illustrates magma eruptions as lava lakes. Figure 23 (bottom right) illustrates pluton cooling/serial magmatism. (top) Extensive cratering would brecciate cumulate layers, mixing and excavating mafic lithologies.

igneous injections and a complex history that would be impossible to resolve on Mars with current observations.

[57] Several alternative possibilities could explain the observed compositions. These include that the basin forming impacts (Argyre, Hellas, Isidis, Utopia or Borealis [*Andrews-Hanna et al.*, 2008]) excavated the mafic cumulates of the lower crust and possibly the upper mantle. The post-overturn upper mantle predicted by *Elkins-Tanton et al.* [2005] would be Mg-rich bearing olivine and pyroxene. Our measurements instead show a range of intermediate to low Mg#. Excavation of an un-overturned or partially overturned mantle unit could produce consistent results but would be unlikely given the gravitational drive of the overturn for the former and the unlikely chance of only sampling the overturned remnants in

the latter. Another option that we will explore in detail is the formation of an igneous secondary crust that would fit the modeled constraints of the overturn and the crustal observations detailed here. The overturn would result in diapirs of Mg-rich cumulates buoyantly rising through the early Martian mantle. These diapirs would have formed from the earliest Martian cumulates, dominated by forsterite (Mg_2SiO_4) and enstatite ($MgSiO_3$). The rising cumulates would experience decompressional melting as the diapir passes the early Martian adiabat forming a partial melt. The initial melting would concentrate on minerals with incompatible elements and the most Fe-rich minerals. Rising diapirs would potentially encounter a proposed garnet-bearing mantle layer near 1050 km depth, providing a source of Al that would facilitate the eventual crystallization of a plagioclase component commonly observed in younger crusts on Mars [*Bandfield et al.*, 2000]. Early crustal observations are consistent with HCP depletion and no garnet detections implying the partial melting of the diapirs past the CPX-out phase of 10% at low pressures [*Walter*, 1998]. The common observation of OPX and olivine suggest a partial melting in the 10–23% range [*Parman and Grove*, 2004]. The resulting melt would be less dense than the rising cumulate diapir and begin its own buoyant accent to the surface. Current observations cannot distinguish between surface eruptions forming lava lakes or near surface intrusions (Figure 23) forming the crust with serial magmatism [*Longhi*, 2003]. Observations only require that the magma bodies are large enough to fractionally crystalize into cumulate layers hundreds to thousands of meters thick and be close enough to the surface to be brecciated and excavated by impact craters. This model of crustal formation explains the observed mineralogically segregated lithologies, the Fe-rich but highly fractionated olivine compositions and the regional differences in composition values that are dependent on minor mantle chemical heterogeneities and varying diapir ascension histories.

6. Conclusions

[58] A planet wide survey of Martian central peaks with well exposed mafic outcrops as determined from CRISM results in 23 examples of deeply excavated Martian crust. The exposures are grouped into three regions in the Southern Highlands; Northern Argyre, Northern Hellas, Nili Fossae and several sites in the Northern Plains. In each of the exposures we observe olivine and/or pyroxene-bearing outcrops, including the impact melt unit, with little spectral evidence of mineral mixing in the VNIR, and the possible occurrence of plagioclase from TIR observations. This suggests that the deep crust is comprised of mineralogically segregated units. Olivine outcrops show a range of compositions from strongly fayalitic to moderately forsteritic. Pyroxene outcrops in the Southern Highlands show a relative enrichment in LCP with the Northern Argyre and Nili Fossae regions being more Mg-rich than the North Hellas sites and the Northern Plains.

[59] While this crust sampling method could be excavating younger igneous rocks emplaced in plutons or dikes, it is unlikely that in each of the examined cases we are only excavating younger material. The general consistency in the observations does not indicate a clear signal that a single exposure is of unique origins. While excavating a younger unit is possible the most likely result on a single plate planet is the excavation of a voluminous ancient crust. The deep crust compositional observations are best explained by a crustal formation model that segregates mafic minerals into cumulate bodies. The global distribution of these materials indicates a planetary scale crustal formation process. One such reasonable driver of such an event would be the decompression partial melting of rising diapirs of Mg-rich mantle cumulates in an early planetary overturn process. This crustal formation process would result in a compositionally stratified ancient crust that would be brecciated, incorporated with subsequent volcanics and aqueous alteration to create the crust we observe today.

[60] **Acknowledgments.** We are very grateful for the fine work of the NASA MRO project team and the fine job by the CRISM Science Operations Center (SOC). This work was supported by NASA through a subcontract with the Applied Physics Lab at Johns Hopkins University. The themes and techniques presented here were greatly improved by conversations with Peter Isaacson and Carle Pieters. The manuscript benefited by suggestions from Sandra Wiseman, Leah Cheek, and Steve Ruff. We thank Ed Cloutis and an anonymous reviewer for substantially improving the manuscript.

References

Adams, J. B. (1974), Visible and near-infrared diffuse reflectance: Spectra of pyroxenes as applied to remote sensing of solid objects in the Solar System, *J. Geophys. Res.*, *79*, 4829–4836, doi:10.1029/JB079i032p04829.

Adams, J. B. (1979), Effects of shock-loading on the reflectance spectra of plagioclase, pyroxene, and glass, *Proc. Lunar Planet. Sci. Conf.*, *10th*, 1–3.

Anderson, J. H., Jr., and K. A. Wickersheim (1964), Near infrared characterization of water and hydroxyl groups on silica surfaces, *Surf. Sci.*, *2*, 252–260, doi:10.1016/0039-6028(64)90064-0.

Andrews-Hanna, J. C., et al. (2008), The Borealis basin and the origin of the Martian crustal dichotomy, *Nature*, *453*, 1212–1215, doi:10.1038/nature07011.

Arvidson, R. E., et al. (2008), Spirit Mars Rover Mission to the Columbia Hills, Gusev Crater: Mission overview and selected results from the Cumberland Ridge to Home Plate, *J. Geophys. Res.*, *113*, E12S33, doi:10.1029/2008JE003183.

Bandfield, J. L., et al. (2000), A global view of Martian Surface Compositions from MGS-TES, *Science*, *287*, 1626–1630, doi:10.1126/science.287.5458.1626.

Bandfield, J. L., D. Rogers, M. D. Smith, and P. R. Christensen (2004), Atmospheric correction and surface spectral unit mapping using Thermal Emission Imaging System data, *J. Geophys. Res.*, *109*, E10008, doi:10.1029/2004JE002289.

Baratoux, D., P. Pinet, A. Gendrin, L. Kanner, J. Mustard, Y. Daydou, J. Vaucher, and J.-P. Bibring (2007), Mineralogical structure of the subsurface of Syrtis Major fom OMEGA observations of lobate ejecta blankets, *J. Geophys. Res.*, *112*, E08S05, doi:10.1029/2007JE002890.

Baratoux, D., et al. (2011), Thermal history of Mars inferred from orbital geochemistry of volcanic provinces, *Nature*, *472*, 338–341.

Bell, P. M., and H. K. Mao (1973), Optical and chemical analysis of iron in Luna 20 plagioclase, *Geochim. Cosmochim. Acta.*, *37*(4), 755–759, doi:10.1016/0016-7037(73)90172-5.

Bertka, C. M. and Y. Fei (1997), Mineralogy of the Martian interior up to core-mantle boundary pressures, *J. Geophys. Res.*, *102*, 5251–5264.

Bibring, J.-P., et al. (1989), Results from the ISM experiment, *Nature*, *341*, 591–593, doi:10.1038/341591a0.

Bibring, J.-P., et al. (2006), Global mineralogical and aqueous Mars history derived from OMEGA/Mars Express data, *Science*, *312*, 400–404, doi:10.1126/science.1122659.

Borg, L. E., and D. S. Draper (2003), A petrogenetic model for the origin and compositional variation of the Martian basaltic meteorites, *Meteorit. Planet. Sci*, *38*, 1713–1731, doi:10.1111/j.1945-5100.2003.tb00011.x.

Bouvier, A., et al. (2008), The case for old basaltic shergottites, *Earth Planet. Sci. Lett.*, *266*, 105–124, doi:10.1016/j.epsl.2007.11.006.

Burns, R. G. (1970), Crystal field spectra and evidence of cation ordering in olivine minerals, *Am. Mineral.*, *55*, 1608–1632.

Burns, R. G. (1974), The polarized spectra of iron in silicates: Olivine a discussion of neglected contributions from Fe2+ ions in M(1) sites, *Am. Mineral.*, *59*, 625–629.

Burns, R. G. (1993), *Mineralogical Applications of Crystal Field Theory*, 2nd ed., 551 pp., Cambridge Univ. Press, Cambridge, U. K., doi:10.1017/CBO9780511524899.

Cahill, J. T. S., P. G. Lucey, and M. A. Wieczorek (2009), Compositional variations of the lunar crust: Results from radiative transfer modeling of central peak spectra, *J. Geophys. Res.*, *114*, E09001, doi:10.1029/2008JE003282.

Cawthorn, R. G. (Ed.) (1996), *Layered Intrusions*, Elsevier, Amsterdam.

Cheek, L. C., et al. (2011), Spectral characteristics of plagioclase with variable iron content: Applications to remote sensing of the lunar crust, *Proc. Lunar Planet. Sci. Conf.*, *42nd*, 1617.

Christensen, P. R., et al. (1992), Thermal emission spectrometer experiment: Mars Observer mission, *J. Geophys. Res.*, *97*, 7719–7734, doi:10.1029/92JE00453.

Christensen, P. R., et al. (2004), The Thermal Emission Imaging System (THEMIS) for the Mars 2001 Odyssey Mission, *Space Sci. Rev.*, *110*, 85–130, doi:10.1023/B:SPAC.0000021008.16305.94.

Clénet, H. (2011), Télédétection hyperspectrale: Minéralogie et pétrologie, Application au volcan Syrtis Major (Mars) et à l'ophiolite d'Oman, Ph.D. thesis, L'Universite de Toulouse, Toulouse, France.

Clénet, H., et al. (2011), A new systematic approach using the Modified Gaussian Model: Insight for the characterization of chemical composition of olivines, pyroxenes and olivine–pyroxene mixtures, *Icarus*, *213*, 404–422, doi:10.1016/j.icarus.2011.03.002.

Cloutis, E. A., and M. J. Gaffey (1991), Pyroxene spectroscopy revisited: Spectral composition corrwlations and relationship to geothermometry, *J. Geophys. Res.*, *96*, 22,809–22,826, doi:10.1029/91JE02512.

Cloutis, E. A., M. J. Galley, T. L. Jackowski, and R. L. Reed (1986), Calibrations of phase abundance, composition, and particle size distributions for olivine-orthopyroxene mixtures from reflectance spectra, *J. Geophys. Res.*, *91*, 11,641–11,653, doi:10.1029/JB091iB11p11641.

Combe, J.-P., P. Launeau, P. Pinet, D. Despan, E. Harris, G. Ceuleneer, and C. Sotin (2006), Mapping of an ophiolite complex by high-resolution visible-infrared spectrometry, *Geochem. Geophys. Geosyst.*, *7*, Q08001, doi:10.1029/2005GC001214.

Crown, D. A., and C. M. Pieters (1985) Spectral properties of plagioclase and pyroxene mixtures, *Proc. Lunar Planet. Sci. Conf.*, *16th*, 158–159.

Debaille, V., A. D. Brandon, Q. Z. Yin, and B. Jacobsen (2007), Coupled ^{142}Nd-^{143}Nd evidence for a protracted magma ocean in Mars, *Nature*, *450*, 525–528, doi:10.1038/nature06317.

Debaille, V., A. D. Brandon, C. O. O'Neill, Q.-Z. Yin, and B. Jacobsen (2009), Early Martian mantle overturn inferred from isotopic composition of nakhlite meteorites, *Nat. Geosci.*, *2*, 548–552, doi:10.1038/ngeo579.

Edwards, C. S., P. R. Christensen, and V. E. Hamilton (2008), Evidence for extensive olivine-rich basalt bedrock outcrops in Ganges and Eos chasmas, Mars, *J. Geophys. Res.*, *113*, E11003, doi:10.1029/2008JE003091.

Ehlmann, B. L., et al. (2009), Identification of hydrated silicate minerals on Mars using MRO-CRISM: Geologic context near Nili Fossae and implications for aqueous alteration, *J. Geophys. Res.*, *114*, E00D08, doi:10.1029/2009JE003339.

Elkins-Tanton, L. T., P. C. Hess, and E. M. Parmentier (2005), Possible formation of ancient crust on Mars through magma ocean processes, *J. Geophys. Res.*, *110*, E12S01, doi:10.1029/2005JE002480.

Fassett, C. I., and J. W. Head III (2005), Fluvial sedimentary deposits on Mars: Ancient deltas in a crater lake in the Nili Fossae region, *Geophys. Res. Lett.*, *32*, L14201, doi:10.1029/2005GL023456.

Flahaut, J., et al. (2011), Dikes of distinct composition intruded into Noachian-aged crust exposed in the walls of Valles Marineris, *Geophys. Res. Lett.*, *38*, L15202, doi:10.1029/2011GL048109.

Francis, D. (2011), Columbia Hill: An exhumed layered igneous intrusion on Mars?, *Earth Planet. Sci.*, *310*, 59–64.

Gillespie, A. R., A. B. Kahle, and R. E. Walker (1986), Color enhancement of highly correlated images. I. Decorrelation and HSI contrast stretches, *Remote Sens. Environ.*, *20*, 209–235, doi:10.1016/0034-4257(86)90044-1.

Head, J. W., III, M. A. Kreslavsky, and S. Pratt (2002), Northern lowlands of Mars: Evidence for widespread volcanic flooding and tectonic deformation in the Hesperian Period, *J. Geophys. Res.*, *107*(E1), 5003, doi:10.1029/2000JE001445.

Hiroi, T., and S. Sasaki (2001), Importance of space weathering simulation products in compositional modeling of asteroids: 349 Dembowska and 449 Aeternitas as examples, *Meteorit. Planet. Sci.*, *36*, 1587–1596, doi:10.1111/j.1945-5100.2001.tb01850.x.

Hoefen, T. M., et al. (2003), Discovery of olivine in the NiliFossae region of Mars, *Science*, *302*, 627, doi:10.1126/science.1089647.

Isaacson, P. J., and C. M. Pieters (2010), Deconvolution of lunar olivine reflectance spectra: Implications for remote compositional assessment, *Icarus*, *210*, 8–13, doi:10.1016/j.icarus.2010.06.004.

Isaacson, P. J., et al. (2011), Remote compositional analysis of lunar olivine-rich lithologies with Moon Mineralogy Mapper (M3) spectra, *J. Geophys. Res.*, *116*, E00G11, doi:10.1029/2010JE003731.

Kanner, L. C., J. F. Mustard, A. Gendrin (2007), Assessing the limits of the Modified Gaussian Model for remote spectroscopic studies of pyroxenes on Mars. *Icarus*, *187*, 442–456, doi:10.1016/j.icarus.2006.10.025 14.

Kelemen, P. B., et al. (1995), Extraction of mid-ocean-ridge basalt from the upwelling mantle by focused flow of melt in dunite channels, *Nature*, *375*, 747–753, doi:10.1038/375747a0.

King, T. V. V., and W. I. Ridley (1987), Relation of the spectroscopic reflectance of olivine to mineral chemistry and some remote sensing implications, *J. Geophys. Res.*, *92*, 11,457–11,469, doi:10.1029/JB092iB11p11457.

Kirk, R. L., et al. (2008), Ultrahigh resolution topographic mapping of Mars with MRO HiRISE stereo images: Meter-scale slopes of candidate Phoenix landing sites, *J. Geophys. Res.*, *113*, E00A24, doi:10.1029/2007JE003000.

Klima, R. L., C. M. Pieers, and M. D. Dyar (2007), Spectroscopy of synthetic Mg-Fe pyroxenes I: Spin-allowed and spin-forbidden crystal field bands in the visible and near-infrared, *Meteorit. Planet. Sci*, *42*, 235–253, doi:10.1111/j.1945-5100.2007.tb00230.x.

Klima, R. L., C. M. Pieters, and M. D. Dyar (2008), Characterization of the 1.2 μm M 1 pyroxene band: Extracting cooling history from near-IR spectra of pyroxenes and pyroxene-dominated rocks, *Meteorit. Planet. Sci*, *43*, 1591–1604, doi:10.1111/j.1945-5100.2008.tb00631.x.

Koeppen, W. C., and V. E. Hamilton (2008), Global distribution, composition, and abundance of olivine on the surface of Mars from thermal infrared data, *J. Geophys. Res.*, *113*, E05001, doi:10.1029/2007JE002984.

Lapen, T. J., et al. (2010), A younger age for ALH84001 and its geochemical link to shergottite sources in Mars, *Science*, *328*, 347–351, doi:10.1126/science.1185395.

Loizeau, T. J., et al. (2010), Stratigraphy in the Mawrth Vallis region through OMEGA HRSC color imagery and DTM, *Icarus*, *205*, 396–418, doi:10.1016/j.icarus.2009.04.018.

Longhi, J. (2003), A new view of lunar ferroan anorthosites: Post magma ocean petrogenesis, *J. Geophys. Res.*, *108*(E8), 5083, doi:10.1029/2002JE001941.

Malin, M. C., et al. (2007), Context Camera Investigation on board the Mars Reconnaissance Orbiter, *J. Geophys. Res.*, *112*, E05S04, doi:10.1029/2006JE002808.

Mangold, N., et al. (2008), Identification of a new outflow channel on Mars in Syrtis Major Planum using HRSC/MEx data, *Planetary Space Sci.*, *56*, 1030–1042.

McEwen, A. S., et al. (2007), Mars Reconnaissance Orbiter's High Resolution Imaging Science Experiment (HiRISE), *J. Geophys. Res.*, *112*, E05S02, doi:10.1029/2005JE002605.

McGuire, P. C., et al. (2009), An improvement to the volcano-scan algorithm for atmospheric correction of CRISM and OMEGA spectral data, *Planet. Space Sci.*, *57*, 809–815, doi:10.1016/j.pss.2009.03.007.

McSween, H. Y. (2002), The rocks of Mars, from far and near, *Meteorit. Planet. Sci*, *37*, 7–25, doi:10.1111/j.1945-5100.2002.tb00793.x.

McSween, H. Y., et al. (2006), Characterization and petrologic interpretation of olivine-rich basalts at Gusev Crater, Mars, *J. Geophys. Res.*, *111*, E02S10, doi:10.1029/2005JE002477.

Melosh, H. J. (1989), *Impact Cratering: A Geologic Process*, Oxford Univ. Press, Oxford, U. K.

Mittlefehldt, D. W. (1994), ALH84001, a cumulate orthopyroxenite member of the Martian meteorite clan, *Meteoritics*, *29*, 214–221, doi:10.1111/j.1945-5100.1994.tb00673.x.

Murchie, S., et al. (2007), Compact Reconnaissance Imaging Spectrometer for Mars (CRISM) on Mars Reconnaissance Orbiter (MRO), *J. Geophys. Res.*, *112*, E05S03, doi:10.1029/2006JE002682.

Mustard, J. F., et al. (2001), Evidence for recent climate change on Mars from the identification of youthful near-surface ground ice, *Nature*, *412*(6845), 411–414, doi:10.1038/35086515.

Mustard, J. F., et al. (2005), Olivine and pyroxene diversity in the crust of Mars, *Science*, *307*, 1594, doi:10.1126/science.1109098.

Mustard, J. F., F. Poulet, J. W. Head, N. Mangold, J.-P. Bibring, S. M. Pelkey, C. I. Fassett, Y. Langevin, and G. Neukum (2007), Mineralogy of the Nili Fossae region with OMEGA/Mars Express data: 1. Ancient impact melt in the Isidis Basin andimplications for the transition from the Noachian to Hesperian, *J. Geophys. Res.*, *112*, E08S03, doi:10.1029/2006JE002834.

Mustard, J. F., B. L. Ehlmann, S. L. Murchie, F. Poulet, N. Mangold, J. W. Head, J.-P. Bibring, and L. H. Roach (2009), Composition, morphology, and stratigraphy of Noachian Crust around the Isidis basin, *J. Geophys. Res.*, *114*, E00D12, doi:10.1029/2009JE003349.

Nash, D. B., and J. E. Conel (1974), Spectral reflectance systematics for mixtures of powdered hypersthene, labradorite, and ilmenite, *J. Geophys. Res.*, *79*(11), 1615–1621, doi:10.1029/JB079i011p01615.

Nyquist, L. E., D. D. Bogard, C.-Y. Shih, A. Greshake, D. Stoffler, and O. Eugster (2001), Ages and geologic histories of Martian meteorites, *Space Sci. Rev.*, *96*, 105–164, doi:10.1023/A:1011993105172.

Pan, C., and D. Rogers (2011), Thermal infrared study of central uplifts of Martian impact craters, Abstract P31D-1721 presented at 2011 Fall Meeting, AGU, San Francisco, Calif., 5–9 December.

Parman, S. W., and T. L. Grove (2004), Harzburgite melting with and without H2O: Experimental data and predictive modeling, *J. Geophys. Res.*, *109*, B02201, doi:10.1029/2003JB002566.

Pelkey, S. M., et al. (2007), CRISM multispectral summary products: Parameterizing mineral diversity on Mars from reflectance, *J. Geophys. Res.*, *112*, E08S14, doi:10.1029/2006JE002831.

Poulet, F., J.-P. Bibring, Y. Langevin, J. F. Mustard, N. Mangold, M. Vincendon, B. Gondet, P. Pinet, J.-M. Bardintzeff, and B. Platevoet (2009), Quantitative compositional analysis of Martian mafic regions using MEx/OMEGA reflectance data: 1. Methodology, uncertainties and examples of application, *Icarus*, *201*, 69–83, doi:10.1016/j.icarus.2008.12.025.

Rogers, A. D., and J. L. Bandfield (2009), Mineralogical characterization of Mars Science Laboratory candidate landing sites from THEMIS and TES, *Icarus*, *203*, 437–453, doi:10.1016/j.icarus.2009.04.020.

Rogers, A. D., and P. R. Christensen (2007), Surface mineralogy of Martian low-albedo regions from MGS-TES data:Implications for upper crustal evolution and surface alteration, *J. Geophys. Res.*, *112*, E01003, doi:10.1029/2006JE002727.

Rogers, A. D., P. R. Christensen, and J. L. Bandfield (2005), Compositional heterogeneity of tha ancient Martian crust: Analysis of Ares Vallis bedrock with THEMIS and TES data, *J. Geophys. Res.*, *110*, E05010, doi:10.1029/2005JE002399.

Ruff, S. W., and P. R. Christensen (2002), Bright and dark regions on Mars: Particle size and mineralogical characteristics basedon Thermal Emission Spectrometer data, *J. Geophys. Res.*, *107*(E12), 5127, doi:10.1029/2001JE001580.

Ruff, S. W., and P. R. Christensen (2007), Basaltic andesite, altered basalt, and a TES-based search for smectite clay minerals on Mars, *Geophys. Res. Lett.*, *34*, L10204, doi:10.1029/2007GL029602.

Ruff, S. W., et al. (2011), Characteristics, distribution, origin, and significance of opaline silica observed by the Spirit rover in Gusev crater, Mars, *J. Geophys. Res.*, *116*, E00F23, doi:10.1029/2010JE003767.

Salvatore, M. R., J. F. Mustard, M. B. Wyatt, and S. L. Murchie (2010), Definitive evidence of Hesperian basalt in Acidalia and Chryse planitiae, *J. Geophys. Res.*, *115*, E07005, doi:10.1029/2009JE003519.

Schultz, P. H., and H. Glicken (1979), Impact crater and basin control of igneous processes on Mars, *J. Geophys. Res.*, *84*(B14), 8033, doi:10.1029/JB084iB14p08033.

Skok, J. R., J. F. Mustard, S. L. Murchie, M. B. Wyatt, and B. L. Ehlmann (2010), Spectrally distinct ejecta in Syrtis Major, Mars: Evidence for environmental change at the Hesperian-Amazonian boundary, *J. Geophys. Res.*, *115*, E00D14, doi:10.1029/2009JE003338.

Squyres, S. W., et al. (2004), The Spirit Rover's Athena science investigation at Gusev Crater, Mars, *Science*, *305*, 794–799, doi:10.1126/science.3050794.

Squyres, S. W., et al. (2006), Rocks of the Columbia Hills, *J. Geophys. Res.*, *111*, E02S11, doi:10.1029/2005JE002562.

Squyres, S. W., et al. (2007), Pyroclastic activity at Home Plate in Gusev Crater, Mars, *Science*, *316*, 738–742, doi:10.1126/science.1139045.

Squyres, S. W., et al. (2008), Detection of silica-rich deposits on Mars, *Science*, *320*, 1063–1067.

Sunshine, J. M., and C. M. Pieters (1993), Estimating modal abundances from modified from spectra of natural and laboratory pyroxene mixtures using the modified Gaussian model, *J. Geophys. Res.*, *98*, 9075–9087, doi:10.1029/93JE00677.

Sunshine, J. M., and C. M. Pieters (1998), Determining the composition of olivine from reflectance spectroscopy, *J. Geophys. Res.*, *103*, 13,675–13,688, doi:10.1029/98JE01217.

Sunshine, J. M., C. M. Pieters, and S. F. Pratt (1990), Deconvolution of mineral absorption bands: An improved approach, *J. Geophys. Res.*, *95*, 6955–6966, doi:10.1029/JB095iB05p06955.

Tarantola, A., and B. Valette (1982), Generalized non-linear inverse problems solved using the least squared criterion, *Rev. Geophys.*, *20*, 219–232, doi:10.1029/RG020i002p00219.

Taylor, S. R. (1992), *Solar System Evolution: A New Perspective*, 307 pp., Cambridge Univ. Press, New York.

Tompkins, S., and C. M. Pieters (2010), Spectral characteristics of lunar impact melts amd inferred mineralogy, *Meteorit. Planet. Sci.*, *45*(7), 1152–1169, doi:10.1111/j.1945-5100.2010.01074.x.

Tornabene, L. L., J. E. Moersch, H. Y. McSween Jr., V. E. Hamilton, J. L. Piatek, and P. R. Christensen (2008), Surface and crater-exposed lithologic units of the Isidis Basin as mapped by coanalysis of THEMIS and TES derived data products, *J. Geophys. Res.*, *113*, E10001, doi:10.1029/2007JE002988.

Tornabene, L. L., et al. (2010), A crater-exposed bedrock database for Mars with applications for determining the composition and structure of the upper crust, *Lunar Planet. Sci.*, *XLI*, Abstract 7137.

Walter, M. J. (1998), Meeting of garnet peridotite and the origin of komatiite and depleted lithosphere, *J. Petrol.*, *39*(1), 29–60, doi:10.1093/petroj/39.1.29.

Warren, P. H. (1990), Lunar anorthosites and the magma-ocean plagioclase-flotation hypotheses: Importance of FeO enrichment in the parent magma, *Am. Min*, *75*, 46–58.

Warren, P. H., P. Claeys, and E. Cedillo-Pardo (1996), Mega-impact melt petrology (Chicxulub, Sudbury, and the Moon): Effects of scale and other factors on potential for fractional crystallization and development of cumulates, in *The Cretaceous-Tertiary Event and Other Catastrophes in Earth History: Boulder, Colorado*, edited by G. Ryder, D. Fastovsky, and S. Gartner, *Spec. Pap. Geol. Soc. Am.*, *307*, 105–124, doi:10.1130/0-8137-2307-8.105.

Wood, J. A., J. S. Dickey, U. B. Marvin, and B. N. Powell (1970), Lunar anorthosites and a geophysical model of the Moon, *Geochim. Cosmochim. Acta*, *1*, supplement, 965–988.

Wyatt, M. B., and H. Y. McSween (2002), Spectral evidence for weathered basalt as an alternative to andesite in the northern lowlands of Mars, *Nature*, *417*, 263–266, doi:10.1038/417263a.